Redox Biology 55 (2022) 102421

Contents lists available at ScienceDirect

Redox Biology

journal homepage: www.elsevier.com/locate/redox

Phospholipid peroxidation inhibits autophagy via stimulating the delipidation of oxidized LC3-PE

Wen Li [a,b,c,d], Lian-Xiang Luo [f], Qing-Qing Zhou [a,c,d], Hai-Biao Gong [a,c,d], Yuan-Yuan Fu [g], Chang-Yu Yan [a,c,d], E. Li [a,c,d], Jie Sun [a,c,d], Zhuo Luo [a,c,d], Zhao-Jun Ding [a,c,d], Qiong-Yi Zhang [a,c,d], Han-Lu Mu [a,c,d], Yun-Feng Cao [e], Shu-Hua Ouyang [a,c,d,e], Hiroshi Kurihara [a,c,d,e], Yi-Fang Li [a,c,d,e], Wan-Yang Sun [a,c,d,e,***], Min Li [g,**], Rong-Rong He [a,c,d,e,h,*]

[a] Guangdong Engineering Research Center of Chinese Medicine & Disease Susceptibility, Jinan University, Guangzhou, 510632, China
[b] Department of Pediatrics, The Affiliated Hospital of Guangdong Medical University, Zhanjiang, 524001, China
[c] International Cooperative Laboratory of Traditional Chinese Medicine Modernization and Innovative Drug Development of Chinese Ministry of Education (MOE), College of Pharmacy, Jinan University, Guangzhou, 510632, China
[d] Guangdong Province Key Laboratory of Pharmacodynamic Constituents of TCM and New Drugs Research, College of Pharmacy, Jinan University, Guangzhou, 510632, China
[e] Joint Laboratory of Dalian Runsheng Kangtai and Jinan University, Jinan University, Guangzhou, 510632, China
[f] The Marine Biomedical Research Institute, Guangdong Medical University, Zhanjiang, Guangdong, 524023, China
[g] School of Pharmaceutical Sciences, Sun Yat-Sen University, Guangzhou, 510006, China
[h] School of Traditional Chinese Medicine, Jinan University, Guangzhou, 510632, China

ARTICLE INFO

Keywords:
Phospholipid peroxidation
Ferroptosis
Autophagy
Microtubule-associated protein light chain 3
Autophagy Related 4B Cysteine Peptidase (ATG4B)
Autophagosomal membrane

ABSTRACT

Phospholipid peroxidation of polyunsaturated fatty acids at the bis-allylic position drives ferroptosis. Here we identify a novel role for phospholipid peroxidation in the inhibition of autophagy. Using *in vitro* and *in vivo* models, we report that phospholipid peroxidation induced by glutathione peroxidase-4 inhibition and arachidonate 15-lipoxygenase overexpression leads to overload of peroxidized phospholipids and culminate in inhibition of autophagy. Functional and lipidomics analysis further demonstrated that inhibition of autophagy was associated with an increase of peroxidized phosphatidylethanolamine (PE) conjugated LC3. We further demonstrate that autophagy inhibition occurred due to preferential cleavage of peroxidized LC3-PE by ATG4B to yield delipidated LC3. Mouse models of phospholipid peroxidation and autophagy additionally supported a role for peroxidized PE in autophagy inhibition. Our results agree with the recognized role of endoplasmic reticulum as the primary source for autophagosomal membranes. In summary, our studies demonstrated that phospholipid peroxidation inhibited autophagy via stimulating the ATG4B-mediated delipidation of peroxidized LC3-PE.

1. Introduction

Macroautophagy (autophagy) is a highly conserved physiological process responsible for the bulk degradation of cytosolic materials via the lysosomal system. Autophagy is modulated by a series of core autophagy-related proteins (ATGs) found in yeast and higher-order organisms including mammals. Among these ATG proteins, the microtubule-associated protein 1A/1B-light chain 3 (LC3), an ortholog of yeast Atg8 is central to autophagosome formation. LC3 is firstly synthesized as a precursor pro-LC3 protein, which is then processed in the cytoplasm by ATG4B to yield LC3-I [1]. LC3-I is further modified by covalent conjugation with phosphatidylethanolamine (PE) to obtain membrane bound LC3-II (LC3-PE). Translocation of LC3-I from an aqueous cytosolic form to a membrane-bound form through lipidation with PE is thus a critical step for phagophore formation [2,3]. While the structure and mechanistic roles of LC3 in autophagy have been

* Corresponding author. Guangdong Engineering Research Center of Chinese Medicine & Disease Susceptibility, Jinan University, Guangzhou, 510632, China.
** Corresponding author. School of Pharmaceutical Sciences, Sun Yat-Sen University, Guangzhou, 510006, China.
*** Corresponding author. Guangdong Engineering Research Center of Chinese Medicine & Disease Susceptibility, Jinan University, Guangzhou, 510632, China.
E-mail addresses: wanyangsun@jnu.edu.cn (W.-Y. Sun), limin65@mail.sysu.edu.cn (M. Li), rongronghe@jnu.edu.cn (R.-R. He).

https://doi.org/10.1016/j.redox.2022.102421
Received 24 June 2022; Received in revised form 17 July 2022; Accepted 21 July 2022
Available online 5 August 2022

investigated in great detail, the nature of the PE molecular species in LC3-II and their potential roles in regulating autophagy remain elusive and warrant further investigation from a lipidomics perspective.

Among the four ATG4 homologs expressed in mammals, ATG4B exhibit the broadest specificity for substrates [4]. Interestingly, ATG4B activity is known to be regulated by redox modification as evidenced by observations that mutation at Cys292 and Cys361 reduces its redox sensitivity and promotes autophagic flux [5]. Coincidentally, compared with free pro-LC3, ATG4B has a stronger affinity for LC3-PE [6], which enables liberation of most of the LC3 from the autophagosome membrane towards the final stage of autophagy [7]. Consequently, excessive or premature cleavage of LC3-PE by ATG4B is expected to prevent autophagy from advancing its full course.

Ferroptosis is a form of iron-catalyzed cell death characterized by a reduction in glutathione peroxidase-4 (GPX4) activity, accompanied with peroxidation of polyunsaturated fatty acids (PUFAs) that leads to accumulation of phospholipid hydroperoxides [8,9]. While the relationship between ferroptosis and autophagy is still debated, preliminary studies have suggested that autophagy is the initiator of ferroptosis through ferritinophagy and chaperone-mediated autophagy (CMA) mechanisms [10,11].

Lipoxygenases (LOXes) are a family of iron-containing enzymes that drive ferroptosis through peroxidation of membrane phospholipids [12]. The lipoxygenase, arachidonate 15-lipoxygenase (ALOX15), oxygenates PUFAs in a free acid form or in a membrane bound form associated with phospholipids to yield 15-hydroperoxyicosa-5,8,11, 13-tetraenoic acid (15S-HpETE) [13]. A previous study revealed that both non-oxidized PE and oxidized PE were substrates for LC3 lipidation, and that ALOX15-deficient cells underwent autophagic dysfunction [14]. The mechanism underlying these observations have however remained elusive. Nor is there any indication as to whether oxidized PE conjugated LC3 (LC3-PE_{ox}) contributes to the autophagic pathway. Given the crucial role for ATG4B in generating and delivering LC3-I in the early stages of the autophagic pathway, and delipidating LC3-PE towards the conclusion of autophagy, these questions have significant relevance to normal physiology and disease pathology.

In the present study, we systematically characterized the role of phospholipid peroxidation in autophagy regulation. We determined that LC3 lipidation (LC3-PE accumulation) was diminished under phospholipid peroxidation conditions induced by RAS-selective lethal small molecule 3 (RSL3), ALOX15 overexpression, and/or GPX4 deprivation. In contrast, inhibiting ALOX15 or overexpressing GPX4 increased LC3 lipidation. We further determined that these observations were related to a higher affinity of ATG4B for LC3-PE-OOH compared with LC3-PE, and that ALOX15 promoted LC3 delipidation to inhibit autophagy by enhancing the affinity of ATG4B to PE-OOH in mammalian cells.

2. Results

2.1. Phospholipid peroxidation-induced by GPX4 inhibition reduces LC3-II formation

Phospholipid peroxidation-induced accumulation of lipid hydroperoxides is one of the most prominent biomarkers for ferroptosis [8,15, 16]. On the other hand, formation of LC3-II, is a key biomarker for autophagy [2,3]. To study the role of phospholipid peroxidation on autophagy, we examined the effects of RSL3, a GPX4 inhibitor and ferroptosis inducer [17], on rapamycin-induced LC3-II formation. Rapamycin induced LC3-II formation under different conditions (Extended Data Fig. 1a). Rapamycin- or FBS starvation-induced autophagy was found to be inhibited by RSL3, which correlated with a reduction in GPX4 expression (Fig. 1 a-d and Extended Data Fig. 1 b, c). We asked whether phospholipid peroxidation has a similar effect on the formation of GABARAP-II, another member of LC3/GABARAP family protein. Expectedly, rapamycin-induced GABARAP-II formation was also inhibited by RSL3 (Extended Data Fig. 1 d, e). This effect may be explained by either an increase in autophagosome biogenesis or a disturbance of autophagic flux. We measured LC3-II/I protein levels in the presence of either the lysosomal ATPase inhibitor bafilomycin A1 (BaF1)-the higher the accumulation of autophagosomes induced by BaF1 treatment, the higher the rate of autophagic flux. Rapamycin significantly increased LC3-II/I levels in *Gpx4*$^{fl/fl}$ MEFs when compared with the control group. In contrast, RSL3 dampened LC3-II/I levels induced by rapamycin in the absence or presence of BaF1, indicating a normal autophagic flux in these cells (Extended Data Fig. 1 f, g).

LC3B, the most studied LC3/GABARAP family protein, is associated with autophagosome development and maturation and is used to monitor autophagic activity [18,19]. We next monitored autophagosome biogenesis by analyzing GFP-LC3 puncta formation by microscopy. The number of GFP-LC3 puncta was initially increased after rapamycin treatment, but then strongly suppressed after RSL3 treatment (Fig. 1e and f). These observations were confirmed using transmission electron microscopy (Fig. 1g). Finally, live cell imaging performed to detect the formation of lipid hydroperoxides using LiperFluo [20] demonstrated a robust LiperFluo fluorescence, accompanied by a significant decrease in autophagy signal in cells pretreated with RSL3 (Fig. 1h and i). These data therefore suggested an inhibitory role for phospholipid peroxidation in autophagy.

Ferroptosis is driven by inactivation of GPX4, which leads to the accumulation of peroxidized phospholipids [21]. To determine whether the inhibition of autophagy is directly induced by phospholipid peroxidation, the formation of LC3-II was followed in cells treated with tamoxifen to suppress GPX4 expression and in cells overexpressing GPX4. Tamoxifen treatment resulted in suppression of GPX4 protein expression (Extended Data Fig. 1h), which correlated with a decrease in LC3-PE (Fig. 1j). Conversely, cells overexpressing GPX4 exhibited an increase in LC3-II/I ratio (Fig. 1 k and l, and Extended Data Fig. 1i and j). Taken together, these results suggested a direct correlation between phospholipid peroxidation and LC3 lipidation with PE to yield LC3-II.

2.2. Peroxidation of phosphatidylethanolamine (PE) diminishes the formation of LC3-II

Previous studies have identified bi- and tri-oxygenated PE species as ferroptotic cell death signals [15]. To investigate whether esterified oxygenated PUFAs are involved in the formation of LC3-PE, we supplemented cells with exogenous arachidonic acid (AA) followed by induction of RSL3 triggered phospholipid peroxidation. The data presented in Fig. 2a showed that AA supplementation resulted in incorporation of PUFA into PE. Lipidomics analysis performed post RSL3 treatment revealed significant levels of oxygenated AA-PE species, including identified PE(38:4)+2O (Fig. 2b). Notably, RSL3 significantly inhibited rapamycin-induced autophagy, which could be further aggravated by AA supplementation (Fig. 2c–g). As AA-containing PE can be catalyzed by LOX to generate 15-hydroperoxy-AA-PE (PE-OOH) (Fig. 2h) [15], we next treated cells with this specific hydroperoxide, to authenticate the role of PE-OOH in inhibition of autophagy. Intriguingly, we observed that PE-OOH could trigger autophagy inhibition with a decreased transition of LC3-I to LC3-II in both *Gpx4*$^{fl/fl}$ MEF and NSC34 cells (Fig. 2i–l). These data indicated that cellular phospholipid peroxidation specifically suppressed LC3-II formation.

2.3. ALOX15-induced PE peroxidation inhibits the formation of LC3-PE

There are different types of lipoxygenases (LOX) that could contribute to oxidation of PUFA. To identify the LOX responsible for RSL3 initiated inhibition of autophagy in the above experiments, inhibition studies were performed using specific LOX inhibitors. Of the inhibitors tested, only the ALOX15 inhibitor, PD146176, prevented the negative effects of RSL3 induced ferroptosis on autophagy (Fig. 3a and b). These observations agreed with immunofluorescence studies that revealed a marked decrease in GFP-LC3 puncta in the presence of RSL3,

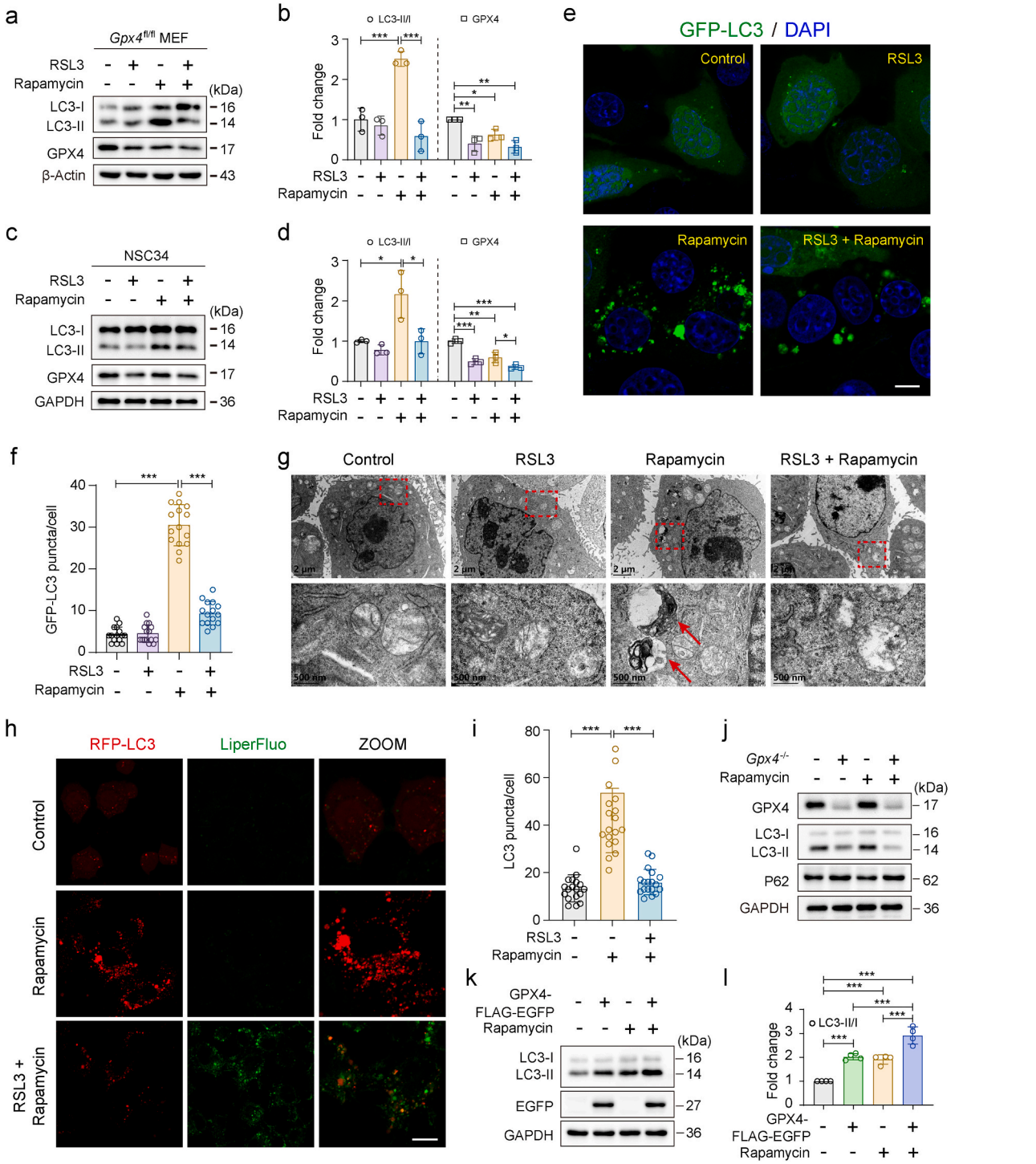

(caption on next page)

Fig. 1. Phospholipid peroxidation induced by RSL3 inhibits autophagy.
a, Immunoblots of LC3 and GPX4 expression in *Gpx4*$^{fl/fl}$ MEF incubated with RSL3 (100 nM, 6 h), rapamycin (50 nM, 12 h) or sequentially incubated with RSL3 and rapamycin (100 nM RSL3, 6 h followed by 50 nM rapamycin, 12 h).
b, Relative densitometric quantitation of LC3-II/I and GPX4 in (a). n = 3 samples.
c, Immunoblots of LC3 and GPX4 expression in NSC34 incubated with RSL3 (100 nM, 6 h), rapamycin (50 nM, 12 h) or sequentially incubated with RSL3 and rapamycin (100 nM RSL3 for 6 h, followed by 50 nM rapamycin for 12 h).
d, Relative densitometric quantitation of LC3-II/I and GPX4 in (c). n = 3 samples.
e, Representative fluorescence micrographs of GFP-LC3 expression (green) in *Gpx4*$^{fl/fl}$ MEFs transiently transfected with GFP-LC3, followed by the indicated treatments as described for (a). Scale bar, 10 μm.
f, GFP-LC3 puncta observed in (e) were counted.
g, TEM images of *Gpx4*$^{fl/fl}$ MEFs treated as described for (a). Top panel showed low magnification. Bottom panel showed magnified images of the areas marked in red in the top panel. Arrows indicated autophagosomes. Scale bars, Top panel 2 μm, Bottom panel 500 nm.
h, Live cell fluorescence imaging of lipid hydroperoxide formation in *Gpx4*$^{fl/fl}$ MEFs using LiperFluo, green. Cells were transiently transfected with RFP-LC3, followed by the indicated treatments as described for (a). Scale bar, 10 μm.
i, RFP-LC3 puncta observed in (h) were counted.
j, Immunoblots of LC3, GPX4 and P62 in *Gpx4*$^{-/-}$ cells after treatment with 50 nM rapamycin for 12 h.
k, Immunoblots of LC3 and EGFP in GPX4 overexpressing *Gpx4*$^{fl/fl}$ MEFs after treatment with 50 nM rapamycin for 12 h.
l, Relative densitometric quantitation of LC3-II/I in (k). n = 4 samples.
Data are mean ± s.d.. *$P < 0.05$, **$P < 0.01$, ***$P < 0.001$ (one-way ANOVA followed by Tukey's multiple comparisons test). (For interpretation of the references to colour in this figure legend, the reader is referred to the Web version of this article.)

that was reversed in the presence of the ALOX15 inhibitor (Fig. 3c and d). Conversely, ALOX15 overexpression inhibited autophagy as evidenced by diminished lipidation of LC3 and increased expression of the P62 protein (Fig. 3e). These results co-related with the ability of LC3 to interact with ALOX15 as determined in immunoprecipitation experiments using GFP-LC3 and ALOX15-FLAG (Fig. 3f). Additionally, we determined that endogenous ALOX15 could interact with LC3-PE (Fig. 3g), likely due to the lower level of LC3-II downregulated by RSL3. Taken together, these results suggest a clear correlation between phospholipid peroxidation inhibition of ALOX15 and promotion of autophagy.

2.4. Peroxidized LC3-PE is preferentially hydrolyzed by ATG4B

ATG4B is a key mediator of LC3 conjugation system required for autophagosome formation, maturation and closure. To identify the role of ATG4B in LC3 delipidation, we determined the effect of the ATG4B inhibitor, FMK-9a [22] on LC3 lipidation (LC3-II formation). Cells were pretreated with RSL3 to induce phospholipid peroxidation in the presence or absence of FMK-9a. The data presented in Fig. 4a demonstrated that presence of the ATG4B inhibitor increased the LC3-PE signal when compared with cells not treated with the inhibitor. Intriguingly, inhibition of ATG4B by FMK-9a promoted LC3 lipidation which could be further downregulated by either RSL3 or ALOX15 overexpression (Fig. 4a and b).

The role of ATG4B in the process of autophagy is mainly concentrated in two aspects: (i) the cleavage of pro-LC3 to LC3-I, and (ii) the delipidation of LC3-II to LC3-I [1,4]. Diverse methods have been used to determine the enzymatic activity of ATG4B, as exemplified by immunoblot according to the altered size of LC3 molecular weight [4]. To better elucidate the function of phospholipid peroxidation on autophagosome formation, we applied *ATG4B* KO (*ATG4B*$^{-/-}$) cells, characterized by its inability to generate LC3-I from pro-LC3. To compensate for the absence of LC3-I, these cells were transfected to express the GFP-LC3^{G120} gene [22]. Lipidated LC3 could be accumulated normally when treated with rapamycin, however, LC3 delipidation (GFP-LC3-II to GFP-LC3-I) could not be further enhanced in the presence or absence of RSL3 since no ATG4B at all (Fig. 4c). The data above prompted us to characterize the cleavage of GFP-LC3-II by ATG4B. We next assessed LC3 lipidation level in *ATG4B* KO cells that were transfected with GFP-LC3^{G120} in the presence of RSL3 and/or ATG4B. In this model, only the delipidation process instead of the priming step should be considered. Notably, the cleavage of oxidized GFP-LC3-PE by ATG4B was stronger than that of non-oxidized LC3-PE, which was manifested as a significant decrease in GFP-LC3-II in the presence of RSL3 (Fig. 4d and e).

Recent studies showed that acyl-coenzyme A synthetases (ACSs) and localized *de novo* phospholipid synthesis in the ER constitute a driving force for autophagic membrane assembly during phagophore expansion [23]. This raised the question as to whether oxidation of ER phospholipids could affect autophagy. To address this, an ALOX15 plasmid designed for targeted expression in the ER was developed (ER-A-LOX15-FLAG-cherry). Overexpression of ALOX15 in *Gpx4*$^{fl/fl}$ MEFs reduced LC3-II (Fig. 4f and g). Furthermore, the cleavage of oxidized LC3-PE by ATG4B seemed to be stronger than that of non-oxidized LC3-PE, which was manifested as a decrease in LC3-II in the presence of ER-ALOX15-FLAG-cherry (Fig. 4h and i). Collectively, we noted that compared with LC3-PE, oxidized LC3-PE was effective substrates for ATG4B.

To address the possibility of specific interactions between ATG4B and LC3, immunoprecipitation experiments were performed. Fig. 4j showed data from such a study confirming specific interactions between LC3 and ATG4B. To understand the relative affinities between LC3-PE and LC3-PE-OOH for ATG4B, total LC3 was enriched by immunoprecipitation (IP) using anti-LC3 antibody (Fig. 4k and l). Lipidated LC3 (LC3-PE) was then oxidized to LC3-PE-OOH using ALOX15 and the difference in affinity between ATG4B and, LC3-PE or LC3-PE-OOH was detected. ALOX15 significantly promoted ATG4B-dependent LC3 delipidation (Fig. 4m, n). Lipidomics analysis further revealed that PE accounted for about 61.1% of the total phospholipids in LC3-PE (Fig. 4o, p). Analysis of the fatty acid composition in PE revealed the appearance of a higher levels of oxidized PE species in the ALOX15-treated groups compared with the control groups suggesting that ATG4B had a higher affinity to LC3-PE-OOH and a lower affinity to LC3-PE (Fig. 4q). From the above evidence, we concluded that ALOX15 promoted the cleavage of LC3-PE-OOH by ATG4B, hence inhibiting autophagy.

2.5. ATG4B shows a higher affinity toward PE-OOH

To obtain molecular insights on the affinity between ATG4B and LC3-PE (oxidized), ligand docking analysis was performed using computational modeling. Both non-oxidized PE and oxidized PE-OOH were seen to preferably bind to the catalytic dyad (His280, Asp278) of ATG4B with a binding energy (ΔG) of −5.56 kcal/mol and −6.33 kcal/mol, respectively (Fig. 5a–c). This difference in affinity is likely attributed to an additional interaction between the polar head of PE-OOH and, Thr7 and Thr10 of ATG4B. We next performed molecular dynamics (MD) simulation [24] to assess the interactions of ATG4B towards PE and PE-OOH. 100 ns MD simulation study was also executed to investigate the conformational stability of PE/PE-OOH in the active site region of ATG4B (His280, Asp278 and Cys74) at 300 K temperature. The MD simulations were analyzed in terms of root mean square deviation

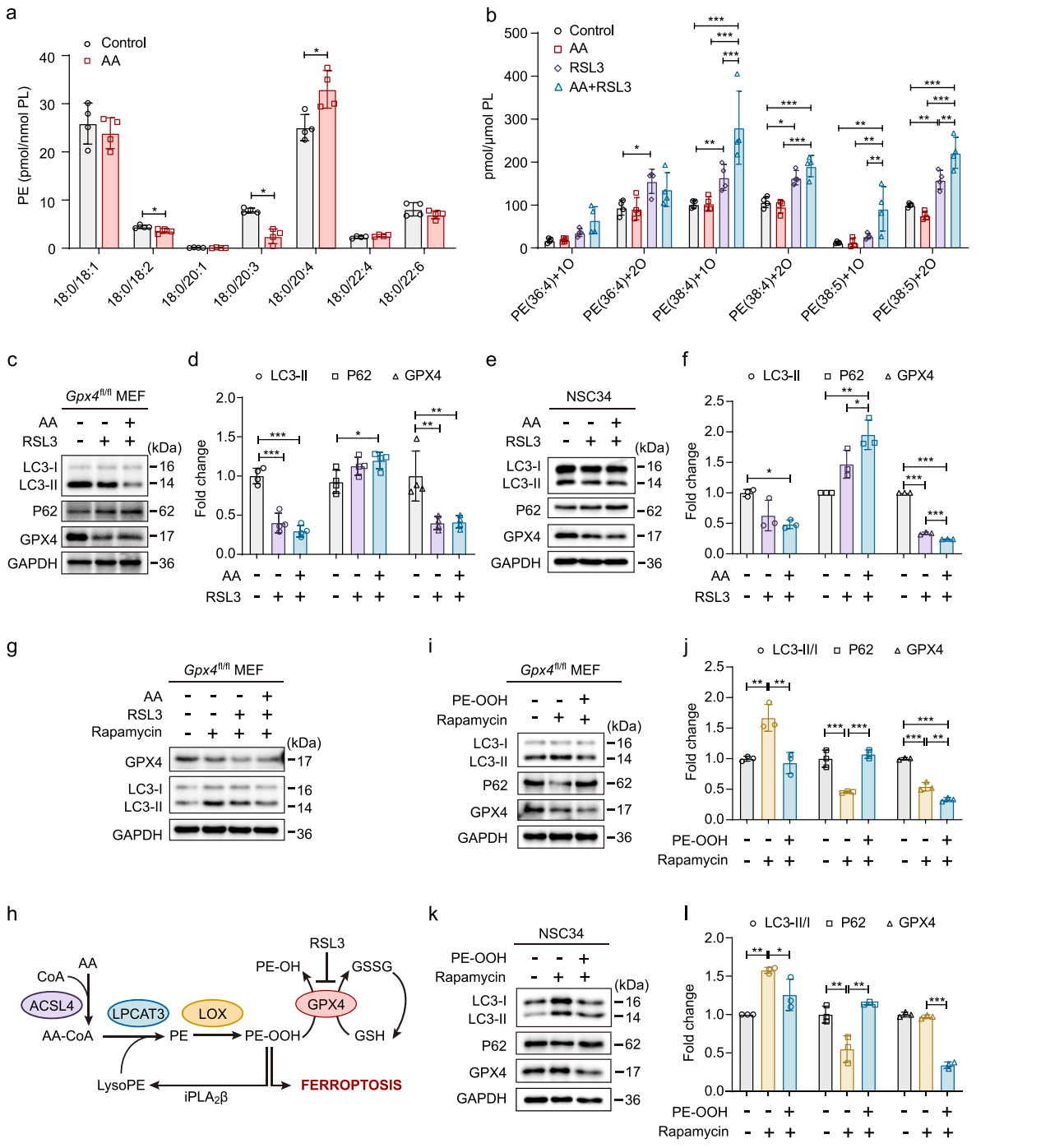

Fig. 2. Peroxized PE diminishes the formation of LC3-II.

a, Quantitative assessment of PE molecular species (sn*1*/sn*2*) in control and AA-supplemented *Gpx4*$^{fl/fl}$ MEFs. n = 4 samples.

b, Quantitative assessment of oxPEs in *Gpx4*$^{fl/fl}$ MEFs treated as indicated. n = 4 samples.

c, Immunoblots showing autophagy inhibition in *Gpx4*$^{fl/fl}$ MEFs treated with RSL3 in the presence of AA.

d, Relative densitometric quantitation of LC3-II, P62 and GPX4 in (c). n = 4 samples.

e, Immunoblot showing autophagy inhibition in NSC34 cells treated with RSL3 in the presence of AA.

f, Relative densitometric quantitation of LC3-II, P62 and GPX4 in (e). n = 3 samples.

g, Immunoblots of cell lysates from *Gpx4*$^{fl/fl}$ MEFs treated as indicated and described in the methods section.

h, AA-initiated metabolic and GPX4-dependent regulation of oxygenated PE ferroptotic signals.

i, Effects of PE-OOH on autophagy in *Gpx4*$^{fl/fl}$ MEFs. Cell lysates were isolated and immunoblotted for the indicated proteins.

j, Relative densitometric quantitation of LC3-II/I, P62 and GPX4 in (i). n = 3 samples.

k, Effects of PE-OOH on autophagy in NSC34 cells. Cell lysates were isolated and immunoblotted for the indicated proteins.

l, Relative densitometric quantitation of LC3-II/I, P62 and GPX4 in (k). n = 3 samples. Student's *t*-test was used for the statistical analysis of (a). Two-way ANOVA with Holm-Sidak's multiple comparisons test was used for the statistical analysis of (b). One-way ANOVA followed by Tukey's multiple comparisons test was used for the statistical analysis of (d, f, j, l). Data are mean ± s.d.. $^{*}P < 0.05$, $^{**}P < 0.01$, $^{***}P < 0.001$.

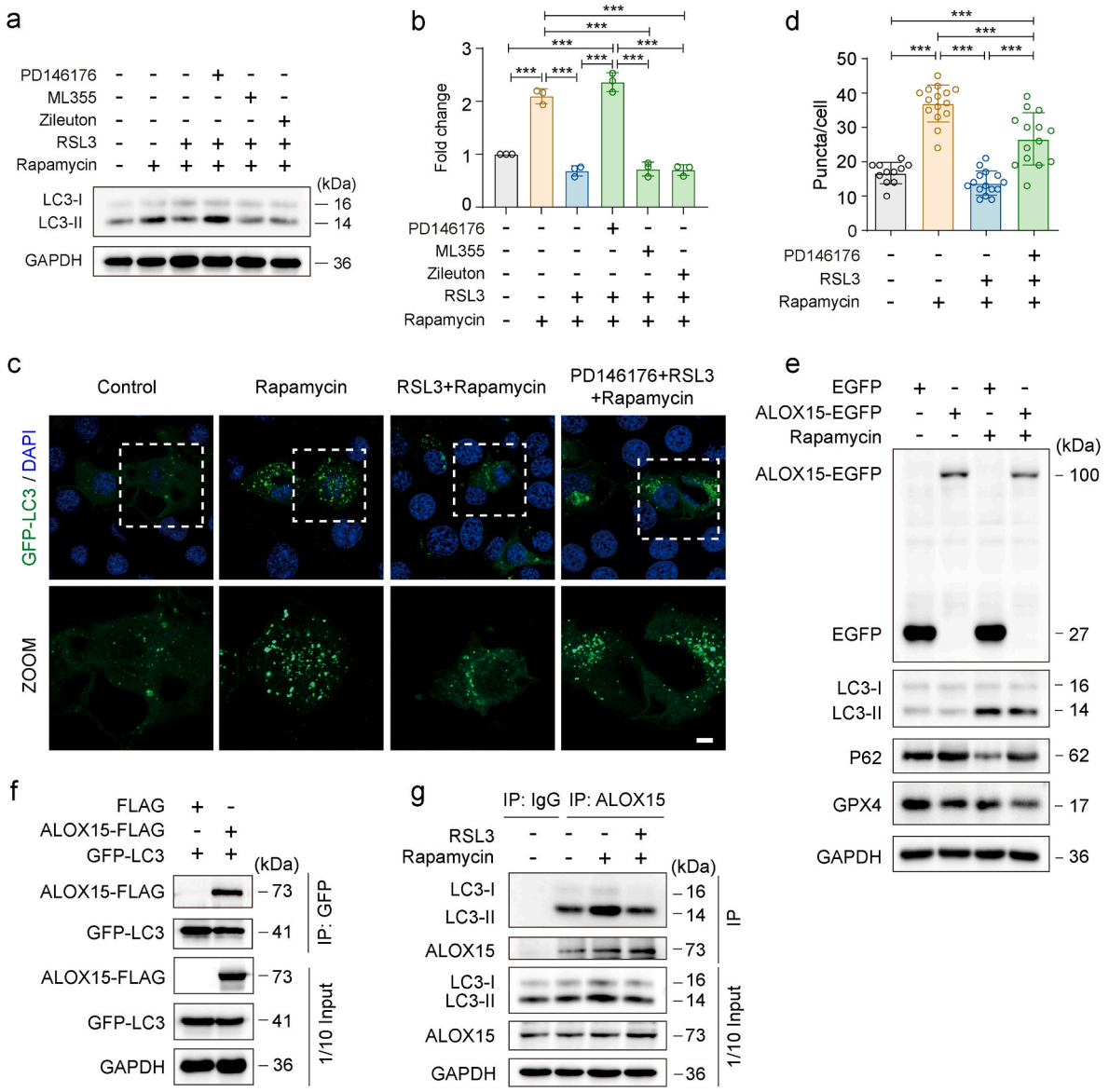

Fig. 3. ALOX15-induced phospholipid peroxidation inhibits the formation of LC3-PE.
a, Effects of LOX inhibitors on autophagy. *Gpx4*$^{fl/fl}$ MEFs were treated with RSL3 and rapamycin as indicated in the absence or presence of the indicated LOX inhibitors followed by immunoblotting of cell lysates.
b, Densitometric quantitation of the ratio of LC3-II to GAPDH in (a). n = 3 samples.
c, *Gpx4*$^{fl/fl}$ MEFs transiently expressing GFP-LC3 (green) were treated with RSL3 and/or rapamycin as indicated before fixation. Scale bar, 10 μm. Top panel showed low magnification. Bottom panel showed magnified images of the marked areas in the top panel.
d, Quantitative analysis of the number of GFP-LC3 puncta observed in (c), counted in randomly selected fields by using ImageJ software.
e, Immunoblots of ALOX15-EGFP overexpressing *Gpx4*$^{fl/fl}$ MEFs after treatment with 50 nM rapamycin for 12 h.
f, Immunoprecipitation of GFP-LC3 and ALOX15-FLAG in *Gpx4*$^{fl/fl}$ MEFs.
g, Immunoprecipitation of LC3 and ALOX15 in *Gpx4*$^{fl/fl}$ MEFs. Data are mean ± s.d.. ***$P < 0.001$ (one-way ANOVA followed by Tukey's multiple comparisons test). (For interpretation of the references to colour in this figure legend, the reader is referred to the Web version of this article.)

(RMSD) and root mean square fluctuations (RMSF) to estimate the variations in the position of the systems in terms of simulation time. Time evolution plot of RMSD of ATG4B and PE/PE-OOH indicated that the system attained stability after 40 ns of simulations. The analysis of ATG4B/PE-OOH complex showed a lower RMSD value than ATG4B/PE, indicating a stronger stability of the atomistic molecular system for the ATG4B/PE-OOH complex. Furthermore, RMSF plot analysis, which represents local changes in the structure of ATG4B upon ligand binding revealed a value in the range of 0.05–0.25, suggestive of low fluctuations in the binding site (Fig. 5d–e). The hydrogen-bonding interactions with the active site region of ATG4B was retained throughout these simulations suggesting the importance of these interactions in stabilizing the simulated complex. Taken together the docking analysis and MD simulations underscored a higher stability of the ATG4B/LC3-PE-OOH complex compared with the ATG4B/LC3-PE complex. While reasons for this disparity between non-oxidized and oxidized PE are unclear, it is speculated that after oxidation, the hydrophobicity of the acyl chains in PE is weakened, thereby making the head group more accessible to the ATG4B protein.

We also performed liposome-binding assay to determine the binding preference of ATG4B towards PE versus PE-OOH. Recombinant ATG4B specifically bound liposomes containing PE or PE-OOH, and showed a relatively higher binding towards PE-OOH versus non-oxidized PE (Fig. 5f). We followed this up with a lipid overlay assay (dot-blot) in

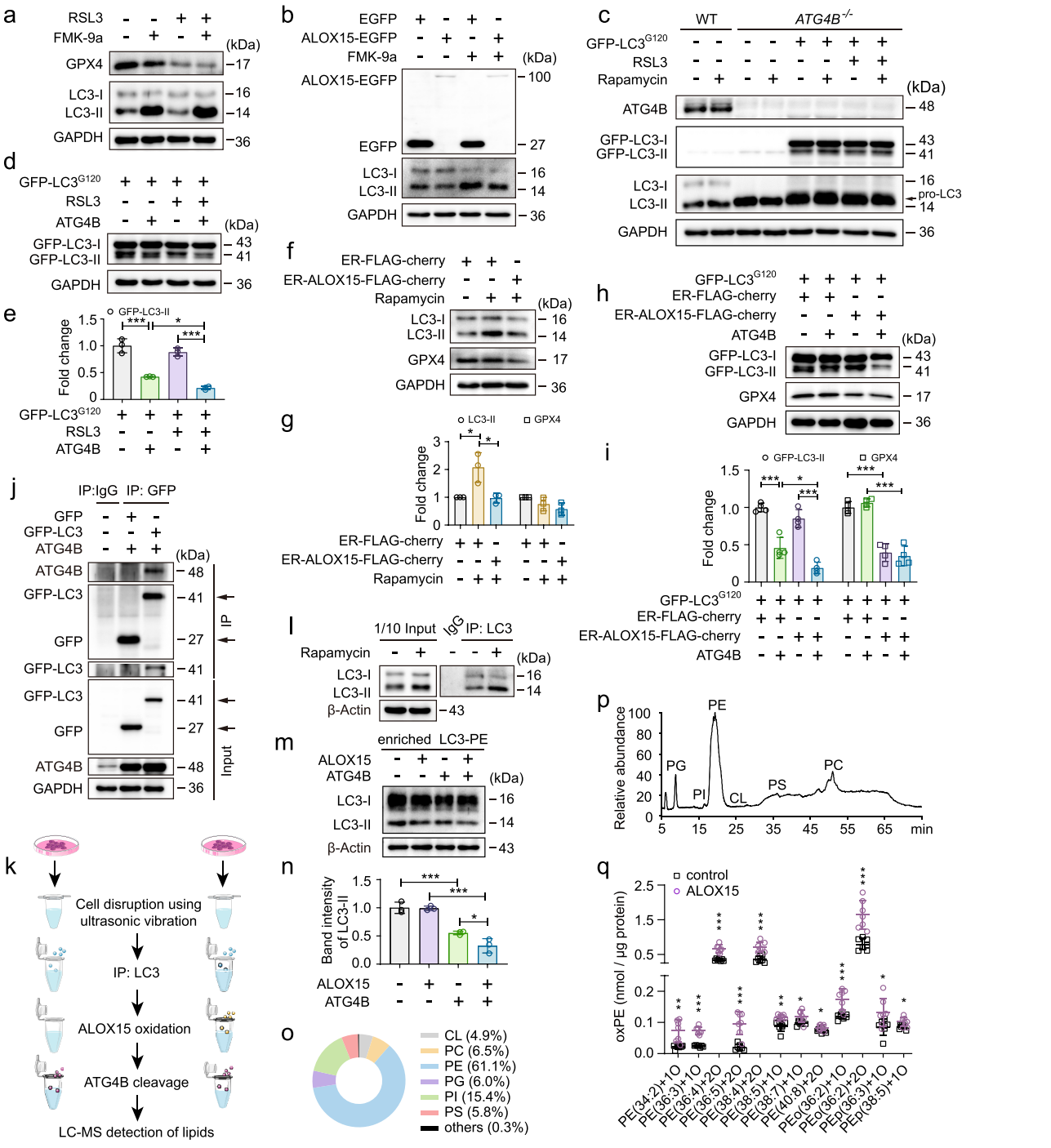

(caption on next page)

Fig. 4. Peroxidized LC3-PE is a preferential substrate for ATG4B.
a, Immunoblots of *Gpx4*$^{fl/fl}$ MEFs treated as described in the methods section.
b, Immunoblots of ALOX15-EGFP overexpressing *Gpx4*$^{fl/fl}$ MEFs after treatment with FMK-9a (1 μM, 6 h).
c, Immunoblots of Hela and *ATG4B* KO Hela (ATG4B$^{-/-}$) with the indicated treatments.
d, ATG4B activity detection by immunoblotting. Cells were treated as indicated, and GFP-LC3 was detected.
e, Relative densitometric quantitation of GFP-LC3-II in (d). n = 3 samples.
f, Immunoblots of ER-ALOX15-FLAG-cherry overexpressing *Gpx4*$^{fl/fl}$ MEFs after treatment with 50 nM rapamycin for 12 h.
g, Relative densitometric quantitation of LC3-II and GPX4 in (f) are shown. n = 3 samples.
h, Detection of ATG4B activity in *ATG4B* KO HeLa cells by SDS-PAGE.
i, Fold changes of GFP-LC3-II and GPX4 in (h). n = 4 samples.
j, Immunoprecipitation of GFP-LC3 and pcDNA3.1(+)-ATG4B in *Gpx4*$^{fl/fl}$ MEFs.
k, Work flow for quantification of PE and oxidation products in LC3-II by LC-MS. Cells were disrupted by sonication and the lysates immunoprecipitated using anti-LC3 antibodies. The pellets were then incubated with ALOX15 to get oxidized PE, followed by incubation with ATG4B to release the lipids for LC-MS analysis.
l, Immunoprecipitation of LC3 in *Gpx4*$^{fl/fl}$ MEFs incubated with 500 nM rapamycin for 14 h.
m, *In vitro* oxidation of LC3-PE by ALOX15 and its enzymatic reaction with ATG4B. Samples were subjected to SDS-PAGE.
n, Band intensity of LC3-II in (m). n = 3 samples.
o, Relative abundance of each class of phospholipids in LC3-II. CL, cardiolipin; PC, phosphatidylcholine; PG, phosphatidylglycerol; PI, phosphatidylinositol; PS, phosphatidylserine.
p, Representative normal-phase LC-MS chromatogram of phospholipids in LC3-II.
q, The amounts of oxidized PE in LC3-II. n = 7 samples.
One-way ANOVA followed by Tukey's multiple comparisons test was used for the statistical analysis of (e, g, i, n). Student's *t*-test was used for the statistical analysis of (q). Data are mean ± s.d.. $^{*}P < 0.05$, $^{**}P < 0.01$, $^{***}P < 0.001$.

which a series of different PE-OOH concentrations was presented and found that this supported the initial impression that ATG4B binds more strongly to PE-OOH (Fig. 5g), in agreement with the MD results reported above. Additionally, the protease activity of ATG4B was positively regulated in the presence of RSL3 with increased cleavage of GFP-LC3-II (Fig. 5h and i). Additionally, cellular thermal shift assay (CETSA) revealed an increased thermal stabilization of ATG4B protein by PE-OOH, relative to PE (Fig. 5 j, k), suggesting a preferentially binding of ATG4B with PE-OOH. In summary, both non-oxidized PE and oxidized PE could act as substrates for LC3 lipidation, but ATG4B showed a higher affinity to PE-OOH (Fig. 5l).

2.6. Phospholipid peroxidation inhibits autophagy in vivo

To better understand the physiological relevance of the *in vitro* results, animal studies were performed. Mice were administered IP injections of RSL3 alone or RSL3 with ferrostatin-1 (Fer-1). Fig. 6a and b and Extended Data Fig. 2a and b showed that treatment with Fer-1 enhanced autophagy as quantified by an increase in LC3-II/I and a decrease in P62. Immunohistochemical analysis revealed that LC3 staining in the midbrain was considerably boosted in the presence of Fer-1 (Extended Data Fig. 2c and d).

Next, we employed another mice model in which RSL3 was intracerebroventricularly injected for two weeks before a single midbrain administration of rapamycin (Extended Data Fig. 3a). Autophagy was induced one day after the rapamycin injection (Extended Data Fig. 2e). Western blot analysis of midbrain tissues showed that RSL3 inhibited rapamycin-induced autophagy as evidenced by a significant decrease in LC3-II/I and an increased P62 (Fig. 6c and d).

ER contributes to phagophore generation and elongation by providing the necessary membrane components [25–27]. To determine whether oxidized lipids in the ER could affect autophagy, purified ER membranes from midbrain tissue of mice-injected with RSL3 were extracted (Fig. 6e) for LC-MS analysis to detect the oxygenated products. Redox phospholipidomics analysis of the ER membranes extracted from the midbrain of mice revealed distinct oxygenated phospholipid profiles in control versus RSL3 treated groups triggered to undergo autophagy by rapamycin (Fig. 6f and Extended Data Fig. 2f–h). A variety of mono-, di- and tri-oxygenated species of phospholipids were elevated in RSL3-treated groups, indicating a potential link between autophagosomes formation and lipidome alterations in the ER. Volcano plot further showed that oxidized PE species were the predominant oxidized phospholipids accumulating in rapamycin-injected mice in the presence of RSL3 (Fig. 6g).

It was previously reported that GPX4 converted phospholipid hydroperoxides to lipid alcohols, and inactivation of GPX4 led to the accumulation of reactive lipid electrophiles [28]. Consequently, AAV--*Cre*-EGFP was injected into the midbrain of *Gpx4*$^{fl/fl}$ mice to knockdown (KD) *Gpx4*. Four weeks after midbrain injection with AAV-*Cre*-EGFP, a single injection of rapamycin was administered (Extended Data Fig. 3b). It should be noted that LC3 lipidation induced by rapamycin was also considerably inhibited in AAV-*Cre*-inducible *Gpx4* KD mice as seen from immunoblot and immunohistological analysis of LC3 (Fig. 6h and i, Extended Data Fig. 2i and j). Purified ER from the midbrain of those groups was also extracted (Fig. 6j) for LC-MS analysis. Redox phospholipidomics analysis of the ER extracted from the midbrain of mice revealed distinguishing oxygenated phospholipid profiles in rapamycin versus AAV-*Cre*-EGFP + rapamycin treated groups. A variety of mono-, di- and tri-oxygenated species of phospholipids showed a trend toward increased levels in AAV-*Cre*-EGFP-treated groups, indicating a potential link between autophagosomes formation and lipidome alterations in ER. Volcano plot further showed that oxidized PE species were the predominant oxidized phospholipid species accumulating in rapamycin-injected mice when GPX4 was conditionally KD (Fig. 6 k, l).

Additionally, to study the potential role of ALOX15 in LC3 lipidation *in vivo*, AAV-ALOX15-EGFP was injected in the midbrain of C57BL/6 mice (Extended Data Fig. 3c). It was observed that overexpressed ALOX15 alleviated autophagy induced by rapamycin, with a significant decrease in LC3-II/I and a considerable increase of P62, and a weaker LC3 staining signal (Fig. 6m, n, Extended Data Fig. 2k and l). In contrast, knockout of *Alox15* significantly enhanced autophagy (Fig. 6o, p, Extended Data Fig. 2m, n and Fig. 3d). Collectively, these *in vivo* data strongly suggested a role for phospholipid peroxidation in inhibition of autophagy.

3. Discussion

PUFAs are indispensable component of biological membranes. PUFAs-contained phospholipids are sensitively to be oxidized by lipoxygenase to produce phospholipid hydroperoxides (PLOOHs), which accelerates the initiation of autoxidation that drives cell death [29]. PLOOHs can be detected in almost all major prototype modes of regulated cell death including apoptosis, necroptosis, ferroptosis, and pyroptosis. Among them, only ferroptosis is characterized by excessive phospholipid peroxidation [30]. Ferroptosis is mainly driven by lethal phospholipid peroxidation caused by abnormal cell metabolism and imbalanced redox homeostasis. The three core hallmarks of ferroptotic cell death defined as oxidation of phospholipids containing PUFAs,

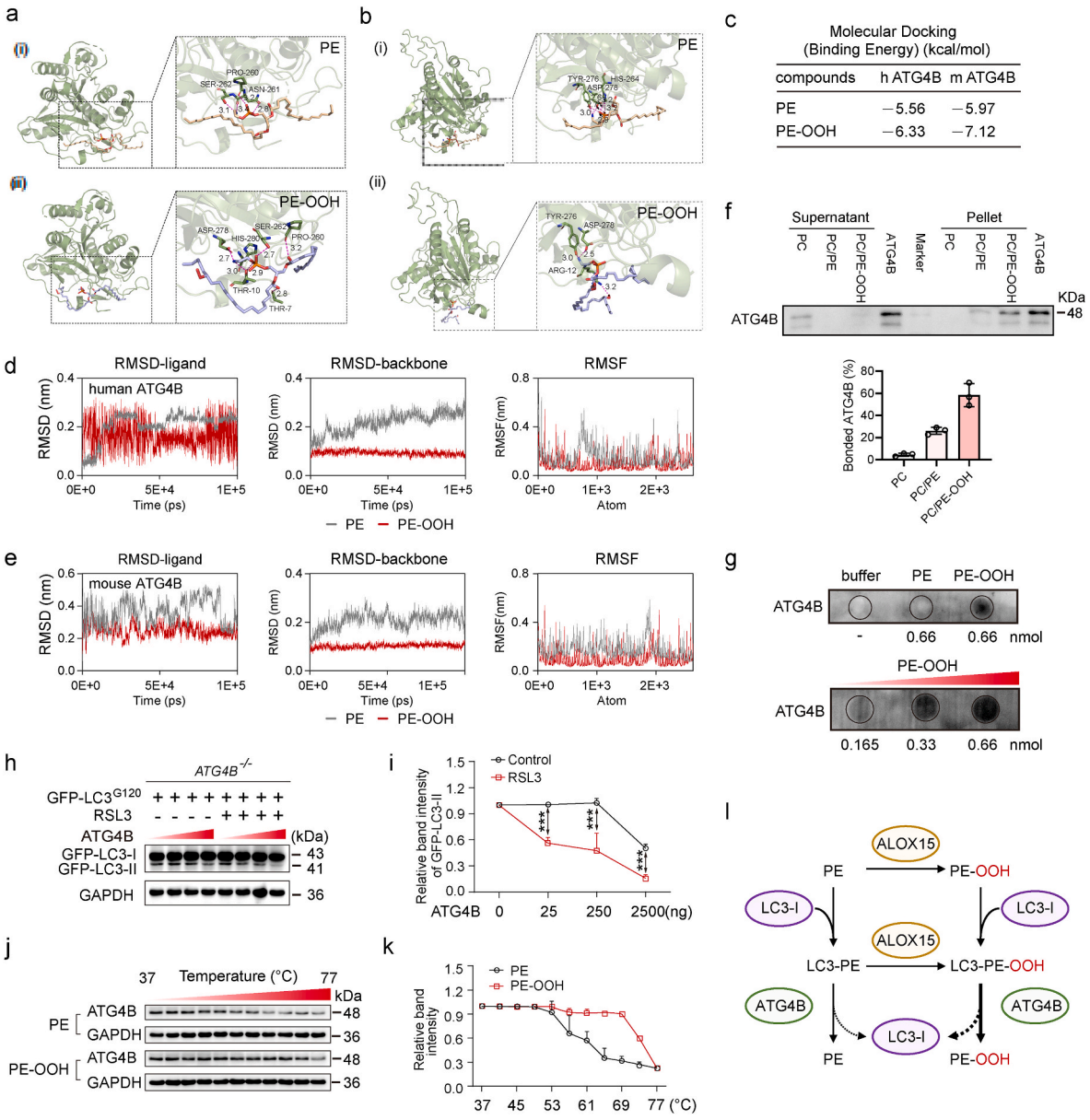

Fig. 5. ATG4B shows a higher affinity for PE-OOH than PE.

a, Ribbon models of human ATG4B (h ATG4B) (ATG4B PDB ID: 2CY7) interactions with PE (i) and PE-OOH (ii).

b, Ribbon models of mouse ATG4B (m ATG4B) interactions with PE (i) and PE-OOH (ii).

c, Binding energies of PE and PE-OOH with h ATG4B and m ATG4B.

d, Molecular dynamics simulation of h ATG4B interacting with PE and PE-OOH.

e, Molecular dynamics simulation of m ATG4B interacting with PE and PE-OOH.

f, Liposome binding assay of ATG4B towards PE and PE-OOH. Recombinant ATG4B (500 ng) was incubated with liposomes (400 nmol) composed of PC, PC/PE (1:1) or PC/PE-OOH (1:1).

g, Dot blot binding analysis of recombinant ATG4B to immobilized PE and PE-OOH.

h, The protease activity of ATG4B is regulated by phospholipid peroxidation.

i, Relative band intensity of GFP-LC3-II for the data shown in (h). n = 3 samples. Differences between the groups were analyzed by two-way ANOVA with Sidak's multiple comparisons test. Data are mean ± s.d.. $^{***}P < 0.001$.

j, Thermal stabilization of ATG4B in *Gpx4*$^{fl/fl}$ MEFs incubated with PE (20 μM, 1 h) and PE-OOH (20 μM, 1 h) was determined using a standard cellular thermal shift protocol with heat treatment from 37 °C to 77 °C.

k, Relative band intensity of ATG4B for the data shown in (j). n = 3 samples. Data are mean ± s.d..

l, A schematic summarizing the role of PE and PE-OOH in the regulation of autophagosome formation. Lipidation of cytoplasmic LC3-I to LC3-II by covalent conjugation of the C-terminal glycine is an essential step for phagophore formation. PE peroxidation induced by ALOX15 results in the formation of oxidized PE, which is also a substrate for LC3-I lipidation. ATG4B shows a higher affinity for PE-OOH than PE.

bioavailability of redox-active iron, and the loss of PL peroxidation repair. It can be prevented by the enzymatic reaction of several major antioxidant systems involving glutathione peroxidase 4 (Gpx4), ferroptosis suppressor protein (FSP1), di/tetrahydrobiopterin (BH_2/BH_4) [28]. We recently revealed that loss function of phospholipase-mediated phospholipid remodeling might be another hallmark of ferroptosis [31]. Overall, the sensitivity of a cell towards ferroptotic cell death is tightly associated with the metabolism of amino acid, iron, and

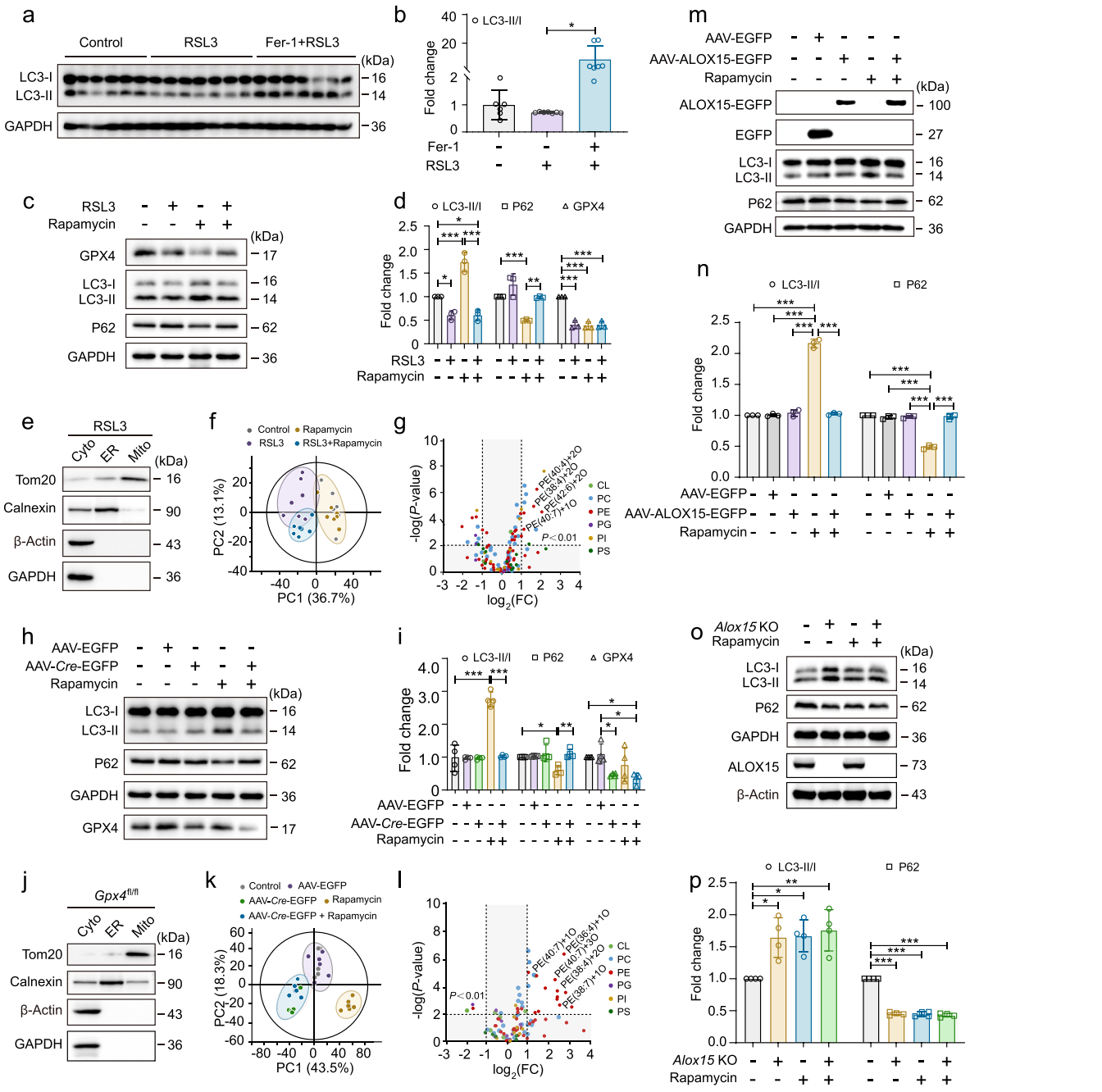

Fig. 6. Phospholipid peroxidation inhibits autophagy *in vivo*.

a, Immunoblot of midbrain tissues of female C57BL/6NCr mice received intraperitoneal injection of RSL3 and Fer-1.

b, Relative densitometric quantitation of LC3-II/I in (a). n = 6–7 samples.

c, Immunoblots of midbrain tissues of male C57BL/6 mice with ICV injection of RSL3 and rapamycin.

d, Relative densitometric quantitation of LC3-II/I, P62 and GPX4 in (c). n = 3 mice.

e, Immunoblots of subcellular fractions from the midbrain tissues of mice in (c). Cyto, cytosol; ER, endoplasmic reticulum; Mito, mitochondria.

f, Score plot of the OPLS-DA. Groups of mice: control, RSL3, rapamycin, RSL3 + rapamycin. n = 7 mice.

g, Volcano plot of the pairwise comparison between rapamycin and RSL3 + rapamycin groups represented by the $\log_2$ (fold change) plotted against the $-\log_{10}$ (*P* value).

h, Immunoblotting of midbrain tissues of $Gpx4^{fl/fl}$ mice with ICV injection of PBS, AAV-EGFP, AAV-*Cre*-EGFP and rapamycin.

i, Relative densitometric quantitation of LC3-II/I, P62 and GPX4 in (h). n = 4 mice.

j, Immunoblots of subcellular fractions from the midbrain tissues of mice in (h).

k, Score plot of the OPLS-DA. Groups of mice: control, AAV-EGFP, AAV-*Cre*-EGFP, rapamycin, AAV-*Cre*-EGFP + rapamycin. n = 6 mice.

l, Volcano plot is represented by the $\log_2$ (fold change) of rapamycin vs AAV-*Cre*-EGFP + rapamycin groups plotted against the $-\log_{10}$ (*P* value).

m, Immunoblotting of midbrain tissues of C57BL/6 mice with ICV injection of PBS, AAV-EGFP, AAV-ALOX15-EGFP and rapamycin.

n, Relative densitometric quantitation of LC3-II/I and P62 in (m). n = 3 mice.

o, Immunoblots of midbrain tissue in WT and *Alox15* KO mice with ICV injection of rapamycin.

p, Relative densitometric quantitation of LC3-II/I and P62 in (o). n = 4 mice. One-way ANOVA followed by Tukey's multiple comparisons test was used for the statistical analysis of (b, d, i, n, p). Data are mean ± s.d.. $^*P < 0.05$, $^{**}P < 0.01$, $^{***}P < 0.001$.

polyunsaturated fatty acid, and also with the biosynthesis of glutathione, phospholipids, NADPH, and coenzyme Q10. Recently, it is found that PLOOHs is not only the executioners of ferroptosis, but also act as the signaling molecules to mediate various biological processes, for example, as the "eat-me" signal on the ferroptotic cell surface to lead the phagocytosis of dead cells [32].

The mutual regulation between ferroptosis and autophagy has attracted the attention of many researchers. Regarding the regulation of autophagy on ferroptosis, it seems that ferroptosis is a type of autophagy-dependent cell death. According to the original study from Dr. Daolin Tang, autophagy contributed to ferroptosis by selective degradation of ferritin to increase iron levels in an ATG5-ATG7-NCOA4 dependent pathway [10]. Additionally, BECN1-induced system xc^- inhibition [33], RAB7A-dependent lipophagy [34], HSP90-associated chaperone-mediated autophagy (CMA) [11], autophagy-dependent SQSTM1-ARNTL-EGLN2-HIF1A pathway [35], and STAT3-mediated lysosomal membrane permeabilization [36] also promoted ferroptosis. The crosstalk between autophagy and ferroptosis revealed a complex interaction between metabolism abnormality and oxidative stress. Hence, finding common characteristic in the mechanisms of autophagy-regulated ferroptosis remains challenging.

High level of ferroptosis not only kills cancer cells but also causes tissue damage. Given that autophagy functions as a double-edged sword-either pro-death or pro-survival, it will be important to delineate whether and how phospholipid peroxidation impacts autophagy as a feedback loop. Research focusing on the elaborate mechanisms regulating autophagy is rapidly growing with regard to the crosstalk between ferroptosis, although much of the results appear contradictory. It has been suggested that phosphatidylethanolamine binding protein 1 (PEBP1) can inhibit autophagy by sequestering LC3 and promoting the generation of ferroptotic mediator PE-OOH when bound to ALOX15. On the contrary, ALOX15 facilitates the lipidation of LC3-I to LC3-II, though the increased LC3-II has no effect on the susceptibility of ferroptosis [37]. An earlier study suggested that ALOX15 disrupted peroxisomal- and mitochondrial-membranes and it could have a role in programmed degradation of peroxisomes and mitochondria [38,39]. As a membranous organelle, can autophagosomes also be affected by ALOX15? Of note, genetic ablation of *Alox15* or pharmaceutical inhibition of ALOX15 promoted autophagy. The increased autophagy by ALOX15 inhibition is a compensatory mechanism for preventing cell damage caused by ALOX15 action [40]. However, the specific mechanism by which autophagy is subsequently activated by ablation or inhibition of ALOX15 is currently unknown. A recent study shows that both native PE and oxidized PE are substrates for LC3 lipidation [14], which is consistent with our results. It was proposed that murine macrophages deficient in ALOX15 resulted in lysosomal storage disorder and defects in autophagy or membrane processing [14]. However, how ALOX15 deficiency leads to altered lysosomes is still an open question. Moreover, 4-hydroxy-2′-nonenal (4-HNE), one of the lipid peroxidation products, can induce autophagy through c-Jun amino-terminal kinase (JNK) [41] and mTOR [42] pathways. On the other hand, 4-HNE also inhibits autophagic flux at higher concentrations [43], demonstrating a negative feedback loop to restrict massive activation of autophagy during lipid peroxidation. GPX4 maintains cellular redox balance by directly reduce phospholipid hydroperoxide. GPX4 is shown to be essential for reticulocyte maturation, and the accumulation of ROS and lipid peroxidation caused by GPX4 depletion lead to impaired reticulocyte maturation and anemia. Mechanistically, autophagy flux and caspase 8 are impaired in the absence of GPX4 [44]. These findings functionally link phospholipid peroxidation with autophagy, yet the mechanism of phospholipid peroxidation in regulating autophagy remains to be studied in depth. Exactly, it remains unknown whether LC3-II molecules having oxidized PE (that is, LC3-PE_{ox}) can be successfully assembled in the phagophore.

In this manuscript, we showed that phospholipid peroxidation induced by RSL3-, AA-/PE–OOH–overload, and ALOX15 overexpression inhibited autophagy *in vitro* and *in vivo*. Conversely, inhibition of ALOX15, or GPX4 overexpression promoted autophagy. Since conjugation of LC3 with PE is a key process for autophagosome formation, we analyzed how LC3 lipidation is regulated. Compared with LC3-PE, LC3-PE_{ox} was an effective substrate for ATG4B cleavage as evidenced by the high oxidized PE content in ALOX15-treated samples (Fig. 4q). The lower binding energy and the higher conformational stability calculated by MD between PE-OOH and ATG4B, suggested a stronger interaction between ATG4B and PE-OOH than between ATG4B and PE (Fig. 5c–e). This was confirmed using a series of binding strength and affinity assays, which showed a preferentially affinity of ATG4B for PE-OOH over PE (Fig. 5f–k). Moreover, phospholipid peroxidation promoted the cleavage of LC3-PE-OOH by ATG4B, hence inhibiting autophagy (Fig. 5l). In conclusion, our study provides evidence that increased phospholipid peroxidation inhibits autophagy via accelerated LC3 delipidation mediated by ATG4B.

Although the mechanistic details remain unclear, the recent advances in our understanding of the mechanisms that drive the biogenesis of autophagosomes have shifted the focus to understanding how cells modulate the redox balance of phospholipids during autophagy. It is presently understood that the endoplasmic reticulum (ER) contributes to PI3P-dependent generation of omegasome, which plays an important role in phagophore generation and elongation [25]. The expansion of precursor membranes of phagophore requires a constant flux of phospholipids that serve as building blocks for membrane biogenesis. Given the high demand for a constant supply of phospholipids during autophagosome formation within a short time, it has been argued that transfer of ER derived phospholipids into autophagic membrane assembly could be one efficient means of meeting this demand [26,27]. Additionally, since the ER membrane is transiently shared with the Golgi, mitochondria and autophagosomes, the contribution of these and other membranes to autophagosome biogenesis is also possible [45–49]. Our data demonstrating that phospholipid peroxidation in ER inhibited autophagy agrees with this concept. We determined that ER-specific phospholipid peroxidation inhibited autophagy *in vitro* (Fig. 4f and g), and ATG4B cleaved more LC3-PE-OOH than LC3-PE in the presence of ER-targeted ALOX15 (Fig. 4h and i). Thus, we showed that ER membranes could be a key source for autophagosome biogenesis in our model. Although we cannot rule out the possibility that several types of other oxidized lipids are also involved in the process, oxPE might be the main source of phospholipids for the formation of autophagosomes.

Studies have implicated several cellular organelles as possible source of the autophagosomal membranes [50,51]. It is improbable that one organelle contributes all the components needed for the assembly of autophagosomal membrane. Even if ER functions as the main source of autophagosomal membrane, whether lipids from other organelles also contribute to the autophagosome formation requires further investigation. Our results indicated that ER is likely an important contributor in the formation of autophagosomes.

The higher affinity of PE-OOH to ATG4B might facilitate the cleavage of LC3-PE-OOH by ATG4B, and led to the formation of LC3-I. Lipidomics analysis revealed that PE accounted for about 61.1% of the total phospholipids in LC3-PE, while PS is only 5.8% (Fig. 4o, p). Although PE was identified as the major lipid conjugated with LC3 *in vivo*, phosphatidylserine (PS) could be also an alternative substrate for its conjugation reaction *in vitro* [52,53]. Hence, whether PS functions as another substrate for LC3 lipidation *in vivo* remains to be answered. Additionally, it has been revealed that LC3 lipidation could be regulated by the PI3K catalytic activity, the ALPS motif of ATG14, and other ATGs in the process of autophagosome maturation [54]. So, besides enhancing the affinity of ATG4B to oxPE, whether other phospholipids peroxidation inhibits autophagy by affecting the above factors merits further studies.

Intracytoplasmic protein misfolding and aggregation is one of the characteristic features of many neurodegenerative diseases (NDs) [55]. Activating the autophagic pathway has become an attractive goal in the treatment of such maladies through the selective degradation of abnormal proteins associated with protein-misfolding disorders.

Growing evidence supports the idea that autophagy disruption at different regulatory steps may also be conducive to the neurodegenerative process [56,57]. For example, elevated ALOX15 protein expression has been detected in patients with Alzheimer's disease (AD) and mild cognitive impairment (MCI), suggesting an early involvement of these in the pathogenesis of AD [58]. In addition, loss of function of ALOX15 prevents the cognitive impairment and the development of AD in a mouse model, implicating ALOX15 might be an AD-relevant molecular target [59,60]. Our results on the negative role for phospholipid peroxidation in autophagy thus raise an intriguing question as to whether phospholipid peroxidation-mediated inhibition of autophagy plays an important role in neurodegeneration.

In conclusion, our approach highlights the potential of combining autophagy induction with ferroptosis induction in an effort to reveal heretofore unrecognized mechanisms that regulate membrane turnover and remodeling in cells. This approach could be readily applied in future studies to dissect the nexus between autophagy and peroxidative damage in cancer and neurodegenerative disease among others.

4. Methods

4.1. Materials

Anti-15Lipoxygenase 1 (Abcam, ab244205), anti-Glutathione Peroxidase 4 (GPX4) (Abcam, ab125066), anti-Calnexin (Proteintech, 10427-2-AP), anti-ATG4B (CST, 13507S), anti-ATG4B (Proteintech, 15131-1-AP), anti-LC3B (CST, 2775), anti-GABARAP (Abgent, AP1821a), anti-SQSTM1/p62 (Abcam, ab56416), anti-GFP (Abcam, ab290), anti-FLAG (Sigma, F1804), anti-Tom20 (Proteintech, 11802-1-AP), anti-GAPDH (Fudebio-tech, FD0063), anti-β-actin (Fudebio-tech, FD0060), normal rabbit IgG (Santa Cruz, sc-2027), goat anti-mouse IgG-HRP (Fudebio-tech, FDM007), goat anti-rabbit IgG-HRP (Fudebio-tech, FDR007), 1*S*, 3*R*-RSL3 (TargetMol, T3646), Fer-1 (Targetmol, T6500), PD146176 (Sigma, P4620), ML355 (Selleck, S6557), Zileuton (Selleck, S1443), Rapamycin (TargetMol, T1537), Bafilomycin A1 (BaF1, Sigma, B1793) Lipofectamine™ LTX Reagent with PLUS™ Reagent (Thermo Fisher Scientific, 15338100), Protein A/G Plus-Agarose Immunoprecipitation Reagent (Santa Cruz, sc-2003), DAPI (Beyotime, C1002), LiperFluo (DOJINDO, L248), Lipoxygenase Inhibitor Screening Assay Kit (Cayman, 760700). PC (1,2-dioleoyl-*sn*-glycero-3-phosphocholine, Avanti, 850375), PE (1-stearoyl-2-eicasotetraenoyl-*sn*-glycero-3-phosphatidylethanolamine, Avanti, 850804), PE-OOH (1-stearoyl-2-15-hydroperoxy-eicasotetraenoyl-*sn*-glycero-3-phosphatidylethanolamine, Cayman, Cay25856-100).

4.2. Plasmids

EGFP, ALOX15-EGFP, FLAG, ALOX15-FLAG, GFP-LC3, RFP-LC3, GPX4-FLAG-EGFP, ER-FLAG-cherry and ER-ALOX15-FLAG-chery were generated and stored in our lab. GFP-LC3^{G120} and pcDNA3.1(+)-ATG4B were generously given by Prof. Min Li (School of Pharmaceutical Sciences, Sun Yat-Sen University). Plasmid Midi Kit (QIAGEN, 12143) was used for plasmids extraction.

4.3. Cell culture and transfection

Gpx4$^{fl/fl}$ MEF was prepared according to our published paper [32]. NSC34 cells were purchased from GuangZhou Jennio Biotech Co.,Ltd. ATG4B$^{-/-}$ HeLa cells used in this paper were prepared before [61]. NSC34 cells were cultured in 1640 medium (Gibco, Grand Island, NY, USA, C11875500BT) supplemented with 10% fetal bovine serum premium (PAN Biotech, Germany, ST30-3302) at 37 °C with 5% CO_2. The other cells used in this paper were cultured in DMEM (Gibco, C11995500BT) supplemented with 10% fetal bovine serum at 37 °C with 5% CO_2. For transfection, Lipofectamine™ LTX Reagent with PLUS™ Reagent was used as per manufacturer's instructions.

4.4. Treatments

For the detection of non-oxidized PE and oxidized PEs, *Gpx4*$^{fl/fl}$ MEFs were individually treated with AA (10 μM, 16 h), RSL3 (1 μM, 6 h), AA (10 μM, 16 h) + RSL3 (1 μM, 6 h). To study the effect of AA + RSL3 on autophagy, *Gpx4*$^{fl/fl}$ MEFs were subjected to the indicated treatments (rapamycin: 50 nM, 12 h; RSL3+rapamycin: 100 nM RS3 for 6 h followed by 50 nM rapamycin for 12 h; AA + RSL3 + rapamycin: 10 μM AA for 16 h + 100 nM RSL3 for 6 h + 50 nM rapamycin for 12 h). To evaluate the effect of PE-OOH on autophagy, *Gpx4*$^{fl/fl}$ MEFs and NSC34 were treated with (1) rapamycin: 100 nM, 12 h; (2) PE-OOH + rapamycin: 1 μM PE-OOH for 8 h, followed by 100 nM rapamycin for 12 h. PD146176 [29], ML355 [62], and Zileuton [29] were used to antagonize ALOX15, ALOX12, and ALOX5, respectively. To inhibit phospholipid peroxidation, 10 μM LOX inhibitors were individually administrated 2 h before RSL3 (100 nM, 6 h), followed by rapamycin incubation (50 nM, 12 h). *Gpx4*$^{fl/fl}$ MEFs were transfected with GFP-LC3, followed by the incubation of rapamycin (50 nM, 12 h), RSL3 (100 nM, 6 h) + rapamycin (50 nM, 12 h), PD146176 (10 μM, 8 h) + RSL3 (100 nM, 6 h) + rapamycin (50 nM, 12 h) before fixation. *Gpx4*$^{fl/fl}$ MEFs were transfected with EGFP or ALOX15-EGFP, followed by the administration of 50 nM rapamycin for 12 h. To detect the interaction between ALOX15 and LC3, *Gpx4*$^{fl/fl}$ MEFs were treated as follows: (1) rapamycin (50 nM, 12 h); (2) RSL3 + rapamycin (100 nM RSL3 for 6 h followed by 50 nM rapamycin for 12 h). *Gpx4*$^{fl/fl}$ MEFs were subjected to the indicated treatments (FMK-9a: 1 μM, 6 h; RSL3: 100 nM, 6 h; RSL3 + FMK-9a: 100 nM RSL3 for 6 h followed by 1 μM FMK-9a for 6 h). *Gpx4*$^{fl/fl}$ MEFs were transfected with EGFP or ALOX15-EGFP, followed by the incubation of 1 μM FMK-9a for 6 h.

4.5. SDS-PAGE and western blotting

Cells were lysed in lysis buffer (Beyotime, P0013) with 1 mM PMSF and protease inhibitors (Roche, 4693116001). After quantification of protein using a protein assay kit (Thermo Fisher Scientific, 23225), equivalent protein were separated by SDS-PAGE and then transferred to PVDF membranes (Merck Millipore, IPVH00010). Membranes were blocked in TBST with 5% skim milk for 1 h at room temperature. Target proteins were detected by overnight incubating with the indicated primary antibodies at 4 °C, followed by the corresponding HRP-conjugated secondary antibodies at room temperature for 2 h. Immunoreactivity was detected with FDbio-Dura ECL kit (Fudebio-tech, FD8020). Membranes were imaged by an automatic chemiluminescence image analysis system (Tanon Science & Technology, Shanghai, Tanon 5200). Band intensity was quantified by ImageJ software.

4.6. Immunoprecipitation

Gpx4$^{fl/fl}$ MEFs were seeded into a 10 cm dish, and treated as indicated. Cells were lysed in lysis buffer (Beyotime, P0013) with 1 mM PMSF and protease inhibitors (Roche, 4693116001) for 30 min on ice. After 10,000 g/min centrifugation for 10 min at 4 °C, the lysates were immunoprecipitated with specific antibody for 6 h at 4 °C, and agarose-protein A/G beads were added subsequently for another 12 h at 4 °C. Thereafter, the beads were washed five times with lysis buffer and boiled in sample buffer for 10 min at 100 °C. Finally, co-precipitated proteins were subjected to immunoblot analysis with indicated antibodies.

4.7. Transmission electron microscopy

Gpx4$^{fl/fl}$ MEFs were subjected to the indicated treatments (control, RSL3: 100 nM, 6 h; rapamycin: 50 nM, 12 h; RSL3 + rapamycin: 100 nM, 6 h RSL3 followed by 50 nM, 12 h rapamycin). For electron microscopy, cells were collected by centrifugation at 800g/min for 3 min. The cell pellet was gently washed once with PBS, and centrifuged again at 800 g/min for 3 min to remove the supernatant. Cells were fixed overnight at

4 °C with 2.5% glutaraldehyde (Millipore, 1.04239.1000-1L) in PBS, and then dehydrated in a graded ethanol series and embedded. Approximately 70 nm ultrathin sections were mounted on nickel grids. The samples were then stained and visualized using a 120 kV JEOL electron microscope (JEM-1400) at 80 kV. Images were captured using a Gatan-832 digital camera [63].

4.8. Immunostaining and confocal microscopy

Cells were seeded on a coverslip to 60% confluence and then transfections were conducted with reference to the suppliers' instruction manual. GFP-LC3 was transfected to each well of a 6-well plate. For immunofluorescence staining, cells were fixed with freshly prepared 4% formaldehyde at 37 °C for 15 min. After washing with PBS, DAPI staining was performed to distinguish the morphology of the nucleus from the cytoplasm. Cell images were captured with a Zeiss800 confocal microscope. GFP/RFP-LC3 puncta was counted in randomly selected fields by using ImageJ software.

4.9. Live-cell imaging of LiperFluo

Gpx4$^{fl/fl}$ MEFs were seeded in 35 mm glass-bottomed tissue culture dishes. RFP-LC3 was transfected for 12 h. Subsequently, cells were subjected to the indicated treatments (rapamycin: 50 nM, 12 h; RSL3 + rapamycin: 100 nM RSL3 for 6 h followed by 50 nM rapamycin for 12 h). Finally, cells were stained with 10 μM LiperFluo for 1 h. Images were acquired using Zeiss800 confocal microscope.

4.10. IHC staining

IHC staining was taken as described in our previous publication [63]. Briefly, paraffin-embedded sections at a thickness of 5 μm were dewaxed in xylene and rehydrated in an alcohol gradient. Antigen retrieval was conducted with 0.01 M sodium citrate buffer (pH = 6.0) by boiling the slices in a microwave for 20 min. Sections were placed in 3% hydrogen peroxide for 30 min to remove endogenous peroxidase activity. To prevent non-specific binding, the sections were blocked by 10% goat serum for 1 h at room temperature in a humidified chamber. Then, the primary antibody (anti-LC3, CST, 2775, 1:100) was added to sections for an incubation at 4 °C overnight. After several washes in PBS, slides were covered with the corresponding secondary antibody at room temperature for 60 min. The secondary antibody was washed off then DAB staining was performed for 10 min in the dark. To visualize nuclei, hematoxylin was added for 5 min. After being dehydrated in an alcohol gradient and vitrified by dimethylbenzene, slides were mounted with coverslips using neutral gum and detected by an automatic scanning microscope (PreciPoint, Freising, Germany).

4.11. Molecular docking

Two-dimensional (2D) structures of PE (1-stearoyl-2-eicasotetraenoyl-*sn*-glycero-3-phosphatidylethanolamine) and PE-OOH (1-stearoyl-2-15-hydroperoxy-eicasotetraenoyl-*sn*-glycero-3-phosphatidylethanolamine) were constructed using ChemOffice to obtain energy-minimized 3D structures. The crystal structure of ATG4B (PDB code: 2CY7) at a resolution of 1.9 Å was used for the virtual screening. The sequence of mouse ATG4B was downloaded from the Uniprot database (Uniprot ID: Q8BGE6). We then used the Swiss-mode (https://swissmodel.expasy.org/) to model the crystal structure of mouse ATG4B. Pymol2.3 and AutoDock4were respectively used to remove water molecules of targets and add hydrogen. Compounds and targets were saved in PDBQT format by AutoDock4. Vina program was then used for docking. Finally, 2D diagrams of the docking complexes of human ATG4B and mouse ATG4B with compounds LC3-PE and LC3-PE-OOH were obtained using Ligplot2.2, and Pymol2.3 was used to draw and analyze the docking complexes and make 3D diagrams.

4.12. Molecular dynamics simulations

ATG4B and compound docking models were analyzed by all atom molecular dynamics (MD) simulations for 100 ns. All the simulations were carried out with Gromacs 2020.2 software package and AMBER99SB-ILDN force field. The force field parameters of PE and PE-OOH were generated by ACPYPE (http://bio2byte.be/). We then set up the box and added the solvent to form a system. To ensure the total charge neutrality of the simulated system, a corresponding amount of sodium ions were added to the system to replace water molecules to produce solvent boxes of the appropriate size. The energy of 50,000 steps in the entire system is minimized (EM) at 300 k. Subsequently, the systems were equilibrated by position restraint simulations of NVT and NPT ensembles. Equilibrated systems were used to simulate 100 ns no restraint production run. Ultimately, MD analyses involving RMSD and RMSF were performed.

4.13. Liposome-binding assay

Liposome-binding assay was performed as described before [64]. In brief, 400 nmol liposomes composed of structural lipid PC, PC/PE (1:1), or PC/PE-OOH (1:1) were incubated with 500 ng of purified ATG4B protein, respectively. Unilamellar vesicles were prepared using a liposome extruder (0.2 μm filters; Avanti Polar Lipids) according to the manufacturer's instructions. Liposomes were diluted in three volumes of binding buffer (150 mM KCl, 25 mM Tris-HCl pH 7.5, 1 mM DTT, 0.5 mM EDTA), pelleted by centrifugation at 60,000 g/min for 15 min, resuspended in 25 μL binding buffer, added to 500 ng purified ATG4B protein, and incubated for 30 min in a total volume of 50 μL at 37 °C. Liposomes were harvested by centrifugation at 16,000 g/min for 30 min, washed once in binding buffer, and then resuspended in Laemmli sample buffer. Samples were separated on SDS-PAGE and immunodetected with ATG4B-specific antibody at 1:1000 (CST, 13507S) after overnight incubation at 4 °C. Thereafter, goat anti-rabbit IgG-HRP (Fudebio-tech, FDR007, 1:5000) was applied as the secondary antibody, and bands were detected with FDbio-Dura ECL kit (Fudebio-tech, FD8020). Membranes were imaged by an automatic chemiluminescence image analysis system (Tanon 5200).

4.14. Lipid dot blot analysis

PE-OOH was immobilized on PVDF membranes. Membranes were blocked in TBST with 5% skim milk at room temperature for 4 h. After 2 × 10 min wash with TBST, membranes were incubated with 25 μg ATG4B recombinant protein that was diluted with TBST at 4 °C overnight. Membranes were washed with TBST for 3 × 10 min. Next, target proteins were immunodetected with ATG4B-specific antibody at 1:1000 (CST, 13507S) after overnight incubation at 4 °C. Thereafter, goat anti-rabbit IgG-HRP (Fudebio-tech, FDR007, 1:5000) was applied as the secondary antibody, and bands were detected with FDbio-Dura ECL kit. Membranes were imaged by an automatic chemiluminescence image analysis system (Tanon 5200).

4.15. Analysis of the ATG4B-mediated cleavage of substrates by SDS-PAGE

The detailed procedure has been described previously [65]. Cells were treated as indicated. (1) HeLa cells were divided into control group and rapamycin group (50 nM, 12 h). *ATG4B* KO HeLa cells were transfected with GFP-LC3^{G120} or not. Cells were then treated with or without rapamycin (50 nM, 12 h) in the presence of RLS3 (100 nM, 12 h) or not. Cell pellets were resuspended in PBS. Lyse the cell pellets by sonication. Subsequently, cell lysates (30 μg) were incubated with purified ATG4B (0.5 μg) at 37 °C for 60 min. The reactions were stopped by the addition of sample buffer. Finally, the substrates and the cleaved products were separated by SDS-PAGE. (2) *ATG4B* KO HeLa cells were transfected with

GFP-LC3^{G120}. Cells were then treated with or without 100 nM RSL3 for 6 h. Cell pellets were resuspended in PBS. Lyse the cell pellets by sonication. Subsequently, cell lysates (30 μg) were incubated with purified ATG4B (0.5 μg) at 37 °C for 60 min. The reactions were stopped by the addition of sample buffer. Finally, the substrates and the cleaved products were separated by SDS-PAGE. (3) GFP-LC3^{G120} was co-transfected with ER-FLAG-cherry or ER- ALOX15-FLAG-cherry into *ATG4B* KO HeLa cells. ATG4B activity was detected by immunoblotting. (4) *ATG4B* KO HeLa cells were transfected with GFP-LC3^{G120}. Cells were then treated with or without 100 nM RSL3 for 6 h. Cell pellets were resuspended in PBS. Lyse the cell pellets by sonication. Subsequently, cell lysates (30 μg) were incubated with different doses of purified ATG4B (0 μg, 0.025 μg, 0.25 μg, 2.5 μg) at 37 °C for 60 min. The reactions were stopped by the addition of sample buffer. Finally, the substrates and the cleaved products were separated by SDS-PAGE.

4.16. Cellular thermal shift assay (CETSA)

Gpx4$^{fl/fl}$ MEFs were harvested and lysed. The supernatants were collected after centrifugation at 10,000 g/min for 15 min and were quantified using Pierce BCA protein assay kit. Cells supernatants were incubated with PE (20 μM, 1 h), and PE-OOH (20 μM, 1 h) at 37 °C for 1 h. Ligand-binding-induced protein thermal stabilization was evaluated followed the melting curve analysis using 37–77 °C gradient for 3 min. After cooling down at room temperature for 3 min, the protein samples were analyzed by western blot analysis.

4.17. In vitro oxidation reaction of LC3-PE mediated by ALOX15

Gpx4$^{fl/fl}$ MEFs were treated with 500 nM rapamycin for 14 h. Cells were resuspended in PBS and sonicated to extract total proteins. To obtain the LC3-PE, 3.3 mg proteins were used for IP using anti-LC3 antibody and protein A/G plus agarose beads. Centrifuge the lysates at 3000 g/min for 3 min and discard the supernatant. Glycine solution (0.1 M, pH = 2.5) was added and gently mixed the beads. The solution was centrifuged at 3000 g/min for 3 min to collect the supernatant. The elution can be adjusted to neutral pH with NaOH immediately and used for further analysis. LC3-PE was oxidized by ALOX15 according to the instruction manual of lipoxygenase inhibitor screening assay kit (Cayman, 760700). Nordihydroguaiaretic acid (NDGA, positive inhibitor of ALOX15) was added to abort the reaction. Subsequently, ATG4B (0.5 μg) was added or not into the mixture and reacted at 37 °C for 60 min. Finally, the mixture was boiled in sample buffer for 10 min at 100 °C, and immunoblotted by denaturing SDS-PAGE.

4.18. Subcellular fractionation

The detailed procedure has been described previously [66,67]. Briefly, midbrains of mice were collected and resuspended in ice-cold IB cells-1 buffer (225 mM mannitol, 75 mM sucrose, 0.1 mM EGTA, and 30 mM Tris-HCl (pH = 7.4)). After gentle homogenization with a dounce homogenizer (about 200 times), tissue extracts were centrifuged at 600 g/min at 4 °C for 5 min to obtain the supernatants. After another centrifugation at 600g/min for 5 min at 4 °C, the supernatants were removed to a new 50 mL polypropylene tube and centrifuged at 7,000 g/min at 4 °C for 10 min to obtain the crude mitochondrial pellet. The supernatants were kept and centrifuged at 100,000 g/min at 4 °C for 1 h to get the ER pellet and cytosolic supernatants. The crude mitochondrial pellet was resuspended gently in 2 mL of ice-cold MRB buffer (250 mM mannitol, 5 mM HEPES (pH = 7.4), and 0.5 mM EGTA) and added on top of 8 mL of percoll medium in an ultracentrifuge tube. MRB solution was then layered gently on top of the mitochondrial suspension to fill the centrifuge tube. Finally, centrifugation was carried out at 95,000 g/min at 4 °C for 1 h to isolate the MAM and pure mitochondria.

4.19. Intraperitoneal (IP) injection of RSL3

Nine-month-old female C57BL/6NCr mice were intraperitoneally anesthetized with 3% sodium pentobarbital. RSL3 was intraperitoneally injected every other day for 3 months (20 mg/kg). Fer-1 (10 mg/kg) was intraperitoneally injected 0.5 h before RSL3. The experimental procedures on animals were conducted in accordance with the Guide for the Care and Use of Laboratory Animals in Jinan University as adopted and promulgated by the United States National Institutes of Health.

4.20. Intracerebroventricular (ICV) injection of RSL3, Fer-1 and rapamycin

Mice were anesthetized with 3% sodium pentobarbital and positioned in a stereotaxic frame. After local sterilization and incision of head skins, the midbrain (1 mm above the substantia nigra, 3.8 mm posterior to the bregma and 1.5 mm lateral from the midline) was localized under a stereotaxic instrument (RWD Life Science Inc., China). After drilling a hole by the high-speed microdrill, a professional animal indwelling needle was fixed on the animal's head with dental cement to facilitate the subsequent continuous injection and provide quick and convenient operation (catheter-single tube/OD 0.48 × ID 0.34 mm/M3.5, catheter cap-single tube/OD 0.30 mm/M3.5, injection tube-single tube/OD 0.30 × ID 0.14 mm/with M3.5, lock tightening nut-single tube/OD 5.5 mm/L7.0 mm/M3.5, PE tube-1.50 × 0.50 mm and screw-SUS304-cross pan head-GB/T 818-M 1.2 × 2.0 mm were customized in RWD Life Science Inc..). To withstand two weeks of ICV injection of drugs, eight-week-old adult mice were used in this model.

(1) RSL3 (dissolved in 2% DMSO, 30% PEG300, 5% Tween 80, 63% H_2O, 2 mg/mL, 3 μL) was slowly injected into the midbrain of eight-week-old male C57BL/6J mice every other day for 2 weeks. Fer-1 (1 mg/mL, 3 μL) was slowly injected into the midbrain 1 d before RSL3 administration.
(2) RSL3 (dissolved in 2% DMSO, 30% PEG300, 5% Tween 80, 63% H_2O, 2 mg/mL, 3 μL) was slowly injected into the midbrain of one-month-old male C57BL/6 mice every other day for 2 weeks. Rapamycin (dissolved in 2% DMSO, 30% PEG300, 5% Tween 80, 63% H_2O, 2.2 mM, 3 μL) was slowly injected into the midbrain on the first day after the last dose of RSL3. Control: solvent only. Mice were sacrificed 1 d after the administration of rapamycin.

4.21. ICV injection of rapamycin

To avoid the influence of age on autophagy level, one-month-old mice were used to establish rapamycin-induced autophagy model. One-month-old *Alox15* KO mice and WT mice were anesthetized with 3% sodium pentobarbital and positioned in a stereotaxic frame. After local sterilization and incision of head skins, the midbrain (1 mm above the substantia nigra, 3.8 mm posterior to the bregma and 1.5 mm lateral from the midline) was localized under a stereotaxic instrument. After drilling a hole by the high-speed microdrill, 500 nL of 2.2 mM rapamycin was respectively injected into the both sides of midbrain at a speed of 90 nL/min using a glass micropipette connected to an ultramicro injection pump (Nanoliter 2010, World Precision Instruments, Sarasota, USA). The micropipette was retained for 5 min before retraction. The head skin was closed for postsurgery monitor. Mice were sacrificed 1 day after the administration of rapamycin.

4.22. ICV injection of AAV-ALOX15-EGFP, AAV-EGFP, AAV-Cre-EGFP

To achieve a good knockout effect of ALOX15 and GPX4, one-two months old mice were used in this model.

(1) One-month-old C57BL/6 mice were anesthetized with 3% sodium pentobarbital and positioned in a stereotaxic frame. After local

sterilization and incision of head skins, the midbrain (1 mm above the substantia nigra, 3.8 mm posterior to the bregma and 1.5 mm lateral from the midline) was localized under a stereotaxic instrument. After drilling a hole by the high-speed microdrill, 250 nL of AAV-ALOX15-EGFP (rAAV-CMV-ALOX15-EGFP-WPRE-pA, serotype 2/9, titer: 2.90×10^{12} vg/mL, BrainVTA (Wuhan) Co., Ltd) or 141.6 nL of AAV-EGFP (rAAV-CMV-EGFP-WPRE-pA, serotype 2/9, titer: 5.12×10^{12} vg/mL, BrainVTA (Wuhan) Co., Ltd) was respectively injected (60 nL/min) into the both sides of the midbrain using a glass micropipette connected to an ultramicro injection pump. The micropipette was retained for 5 min before retraction. The head skin was closed for postsurgery monitor. Rapamycin (2.2 mM, 500 nL) was respectively injected into the both sides of midbrain at a speed of 90 nL/min using a glass micropipette connected to an ultramicro injection pump 1 month after the AAV injection. Control: solvent only. All mice were sacrificed 1 day after the administration of rapamycin.

(2) One-month-old $Gpx4^{fl/fl}$ mice were anesthetized with 3% sodium pentobarbital and positioned in a stereotaxic frame. After local sterilization and incision of head skins, the midbrain (1 mm above the substantia nigra, 3.8 mm posterior to the bregma and 1.5 mm lateral from the midline) was localized under a stereotaxic instrument. After drilling a hole by the high-speed microdrill, 250 nL of AAV-*Cre*-EGFP (rAAV-hSyn-*Cre*-EGFP-WPRE-hGH pA, serotype 2/9, titer: 3.21×10^{12} vg/mL, BrainVTA (Wuhan) Co., Ltd) or 156.7 nL of AAV-EGFP (rAAV-hSyn -EGFP-WPRE-hGH pA, serotype 2/9, titer: 5.12×10^{12} vg/mL, BrainVTA (Wuhan) Co., Ltd) was respectively injected (60 nL/min) into the both sides of the midbrain using a glass micropipette connected to an ultramicro injection pump. The micropipette was retained for 5 min before retraction. The head skin was closed for postsurgery monitor. Rapamycin (2.2 mM, 500 nL) was respectively injected into the both sides of midbrain at a speed of 90 nL/min using a glass micropipette connected to an ultramicro injection pump 1 month after the AAV injection. Control: solvent only. All mice were sacrificed 1 day after the administration of rapamycin.

4.23. Lipid extraction and analysis

Lipids were extracted according to the reported Folch procedure [68]. Global redox phospholipidomics was performed as previously described [31,32]. Phospholipids were analyzed by LC-MS using a Dionex Ultimate 3000 HPLC system coupled with a Q-Exactive Hybrid Quadrupole-Orbitrap mass spectrometer (Thermo Fisher Scientific) using a normal phase column (Luna 3 μm Silica (2) 100 Å, 150 × 2.0 mm, (Phenomenex)). The column was maintained at 35 °C. The analysis was performed using gradient solvents (A and B) containing 10 mM ammonium formate at a flow rate of 0.2 mL/min. Solvent A contained isopropanol/hexane/water (285:215:5, V/V/V), and solvent B contained isopropanol/hexane/water (285:215:40, V/V/V). All solvents were LC/MS-grade. The gradient elution program was set as follows: 0 min, 10% B; 23 min, 32%; 32 min, 65%; 35 min, 100%; 70 min, 100%. Analysis was performed in negative ion mode at a resolution of 70,000 for the full MS scan and 17,500 for the MS [2] scan in data-dependent mode. The scan range for MS analysis was m/z 400–1,800 with a maximum injection time of 200 ms using 1 microscan. Capillary spray voltage was set at 3.0 kV, and capillary temperature was 320 °C. The S-lens Rf level was set to 60. A maximum injection time of 500 ms was used for MS [2] (high-energy collisional dissociation (HCD)) analysis with collision energy set to 24. An isolation window of 1.0 Da was set for the MS and MS [2] scans.

Analysis of raw LC-MS data was performed using Compound Discoverer 2.0 (Thermo Fisher Scientific) with an in-house generated analysis workflow and database. Peaks with a signal-to-noise ratio of more than three were identified and searched against an oxidized PL database. Values for m/z were matched within 5 ppm to identify the lipid species. Lipids were further filtered by retention time and confirmed by MS [2] analysis with the fragments used for their identification (https://www.lipidmaps.org/). Quantitative analysis is based on calibration curves generated by known amounts of reference standards (CL(16:0/18:2/18:2/20:4), PA(18:1/18:1), PC(18:1/18:1), PE (18:1/18:1), PG(18:1/18:1), PI(18:1/18:1), PS(18:1/18:1)) and their corresponding internal standards (CL(14:0/14:0/14:0/14:0), PA (16:0-d31/18:1), PC(16:0-d31/18:1), PE(16:0-d31/18:1), PG (16:0-d31/18:1), PI(16:0-d31/18:1), PS(16:0-d31/18:1)). The *sn*-position of PE was assigned based on the intensities of carboxylate anions and the $[LPE-H]^-$ fragments in MS/MS spectra. As reported [69,70], the carboxylate anion and the $[LPE-H]^-$ fragments derived from the fragmentation at the *sn*-2 position of PE are prominent.

4.24. Statistical analysis

Phospholipids were quantified from full-scan LC/MS spectra with ratiometric comparison to the preselected internal standard using a corresponding standard curve for each phospholipid class. Orthogonal partial least-squares discriminant analysis (OPLS-DA) was performed using SIMCA 13.0 software (Umetrics). The criteria for confirming a potential biomarker were: (i) variable importance in projection (VIP) greater than 1, (ii) fold change >2.0), (iii) two-tailed Student's *t*-test, $P < 0.01$.

All statistics were performed using GraphPad Prism 8 software. Differences between the groups were analyzed by one-way ANOVA with Tukey's *post hoc* analyses, two-way ANOVA with Sidak's multiple comparisons test, or two-way ANOVA with Holm-Sidak's multiple comparisons test. For all experiments, data presented are mean ± s.d.. Designation for significance are as follows; $^*P < 0.05$, $^{**}P < 0.01$, $^{***}P < 0.001$. Graphics were generated using GraphPad Prism 8 and Excel.

Author contributions

RR He conceived and supervised the overall project; M Li and WY Sun revised the manuscript; YF Li, H Kurihara. and YF Cao consulted and assisted in supervising this project; W Li designed and performed *in vitro* and *in vivo* studies, performed and analyzed the electron microscopy data, prepared all the samples for lipidomics analysis, wrote the manuscript and drafted the figures; WY Sun and HB Gong performed and analyzed mass spectrometry studies; LX Luo and WY Sun performed computation analyses; QQ Zhou performed the study of Fig. 3c and d; E Li contributed to Fig. 5f; J Sun, QQ Zhou and HL Mu assisted in providing the reagents; Z Luo and CY Yan assisted in the data interpretation. YY Fu prepared the ATG4B recombinant protein. ZJ Ding, QQ Zhou, J Sun and SH Ouyang assisted in raising mice and some surgical sutures.

Funding

This work was supported, in part, by the National Key Research and Development Program of China (grant number 2017YFC1700404), Natural Science Foundation of China (grant numbers 82125038, 81873209, 32100602, 81622050, 81573675, U1801284, 81673709, 81703696, 31970699, 32100610), the Local Innovative and Research Teams Project of Guangdong Pearl River Talents Program (grant number 2017BT01Y036) and GDUPS (2019), GuangDong Basic and Applied Basic Research Foundation (grant number 2021B1515120023) , the Innovation Team Project of Guangdong Provincial Department of Education (grant number 2020KCXTD003), the Science and Technology Program of Guangzhou (grant number 201903010062).

Data and materials availability

All data needed to evaluate the conclusions in the paper are present in the paper and/or the Supplementary Materials. Additional data

related to this paper may be requested from the authors.

Declaration of competing interest

The authors declare that they have no known competing financial interests or personal relationships that could have appeared to influence the work reported in this paper.

Data availability

Data will be made available on request.

Acknowledgements

We thank all authors for commenting on the manuscript.

Appendix A. Supplementary data

Supplementary data to this article can be found online at https://doi.org/10.1016/j.redox.2022.102421.

References

[1] I. Tanida, et al., HsAtg4B/HsApg4B/autophagin-1 cleaves the carboxyl termini of three human Atg8 homologues and delipidates microtubule-associated protein light chain 3- and GABAA receptor-associated protein-phospholipid conjugates, J. Biol. Chem. 279 (2004) 36268–36276.
[2] N.N. Noda, Y. Fujioka, T. Hanada, Y. Ohsumi, F. Inagaki, Structure of the Atg12-Atg5 conjugate reveals a platform for stimulating Atg8-PE conjugation, EMBO Rep. 14 (2013) 206–211.
[3] M. Walczak, S. Martens, Dissecting the role of the Atg12-Atg5-Atg16 complex during autophagosome formation, Autophagy 9 (2013) 424–425.
[4] M. Li, et al., Kinetics comparisons of mammalian Atg4 homologues indicate selective preferences toward diverse Atg8 substrates, J. Biol. Chem. 286 (2011) 7327–7338.
[5] X.P. Zheng, et al., The protease activity of human ATG4B is regulated by reversible oxidative modification, 1838-185, Autophagy 16 (2020).
[6] N. Fujita, et al., An Atg4B mutant hampers the lipidation of LC3 paralogues and causes defects in autophagosome closure, Mol. Biol. Cell 19 (2008), 4651-465.
[7] T. Noda, N. Fujita, T. Yoshimori, The late stages of autophagy: how does the end begin? Cell Death Differ. 16 (2009) 984–990.
[8] M. Conrad, D.A. Pratt, The chemical basis of ferroptosis, Nat. Chem. Biol. 15 (2019) 1137–1147.
[9] B.R. Stockwell, X. Jiang, W. Gu, Emerging mechanisms and disease relevance of ferroptosis, Trends Cell Biol. 30 (2020) 478–490.
[10] W. Hou, et al., Autophagy promotes ferroptosis by degradation of ferritin, Autophagy 12 (2016) 1425–1428.
[11] Z.M. Wu, et al., Chaperone-mediated autophagy is involved in the execution of ferroptosis, P Natl Acad Sci USA 116 (2019) 2996–3005.
[12] W.S. Yang, et al., Peroxidation of polyunsaturated fatty acids by lipoxygenases drives ferroptosis, P Natl Acad Sci USA 113 (2016) E4966–E4975.
[13] Y.B. Joshi, P.F. Giannopoulos, D. Pratico, The 12/15-lipoxygenase as an emerging therapeutic target for Alzheimer's disease, Trends Pharmacol. Sci. 36 (2015) 181–186.
[14] A.H. Morgan, et al., A novel role for 12/15-lipoxygenase in regulating autophagy, Redox Biol. 4 (2015) 40–47.
[15] V.E. Kagan, et al., Oxidized arachidonic and adrenic PEs navigate cells to ferroptosis, Nat. Chem. Biol. 13 (2017) 81–90.
[16] J. Zheng, M. Conrad, The metabolic underpinnings of ferroptosis, Cell Metabol. 32 (2020) 920–937.
[17] W.S. Yang, B.R. Stockwell, Synthetic lethal screening identifies compounds activating iron-dependent, nonapoptotic cell death in oncogenic-RAS-harboring cancer cells, Chem. Biol. 15 (2008) 234–245.
[18] M.B. Schaaf, T.G. Keulers, M.A. Vooijs, K.M. Rouschop, LC3/GABARAP family proteins: autophagy-(un)related functions, Faseb. J. 30 (2016) 3961–3978.
[19] D.J. Klionsky, et al., Guidelines for the use and interpretation of assays for monitoring autophagy (4th edition)(1), Autophagy 17 (2021) 1–382.
[20] K. Yamanaka, et al., A novel fluorescent probe with high sensitivity and selective detection of lipid hydroperoxides in cells, RSC Adv. 2 (2012) 7894–7900.
[21] I. Ingold, et al., Selenium utilization by GPX4 is required to prevent hydroperoxide-induced ferroptosis, Cell 172 (2018) 409–422.
[22] J. Chu, et al., ATG4B inhibitor FMK-9a induces autophagy independent on its enzyme inhibition, Arch. Biochem. Biophys. 644 (2018) 29–36.
[23] M. Schutter, P. Giavalisco, S. Brodesser, M. Graef, Local fatty acid channeling into phospholipid synthesis drives phagophore expansion during autophagy, Cell 180 (2020) 135–149.
[24] P. Sneha, C.G. Doss, Molecular dynamics: new frontier in personalized medicine, Adv Protein Chem Struct Biol 102 (2016) 181–224.
[25] E.L. Axe, et al., Autophagosome formation from membrane compartments enriched in phosphatidylinositol 3-phosphate and dynamically connected to the endoplasmic reticulum, J. Cell Biol. 182 (2008) 685–701.
[26] S. Maeda, C. Otomo, T. Otomo, The autophagic membrane tether ATG2A transfers lipids between membranes, Elife 8 (2019), e45777.
[27] M. Graef, Recent advances in the understanding of autophagosome biogenesis, F1000Res 9 (2020). F1000 Faculty Rev-212.
[28] X. Jiang, B.R. Stockwell, M. Conrad, Ferroptosis: mechanisms, biology and role in disease, Nat. Rev. Mol. Cell Biol. 22 (2021) 266–282.
[29] R. Shah, M.S. Shchepinov, D.A. Pratt, Resolving the role of lipoxygenases in the initiation and execution of ferroptosis, ACS Cent. Sci. 4 (2018) 387–396.
[30] B. Wiernicki, et al., Excessive phospholipid peroxidation distinguishes ferroptosis from other cell death modes including pyroptosis, Cell Death Dis. 11 (2020) 922.
[31] W.Y. Sun, et al., Phospholipase iPLA2beta averts ferroptosis by eliminating a redox lipid death signal, Nat. Chem. Biol. 17 (2021) 465–476.
[32] X. Luo, et al., Oxygenated phosphatidylethanolamine navigates phagocytosis of ferroptotic cells by interacting with TLR2, Cell Death Differ. 28 (2021) 1971–1989.
[33] X. Song, et al., AMPK-mediated BECN1 phosphorylation promotes ferroptosis by directly blocking system xc(-) activity, Curr. Biol. 28 (2018) 2388–2399.
[34] Y. Bai, et al., Lipid storage and lipophagy regulates ferroptosis, Biochem. Biophys. Res. Commun. 508 (2019) 997–1003.
[35] M. Yang, et al., Clockophagy is a novel selective autophagy process favoring ferroptosis, Sci. Adv. 5 (2019) eaaw2238.
[36] H. Gao, et al., Ferroptosis is a lysosomal cell death process, Biochem Bioph Res Co 503 (2018) 1550–1556.
[37] J.M. Zhao, et al., PEBP1 acts as a rheostat between prosurvival autophagy and ferroptotic death in asthmatic epithelial cells, P Natl Acad Sci USA 117 (2020) 14376–14385.
[38] S. Yokota, T. Oda, H.D. Fahimi, The role of 15-lipoxygenase in disruption of the peroxisomal membrane and in programmed degradation of peroxisomes in normal rat liver, J. Histochem. Cytochem. 49 (2001) 613–622.
[39] S. Pallast, K. Arai, X.Y. Wang, E.H. Lo, K. van Leyen, 12/15-Lipoxygenase targets neuronal mitochondria under oxidative stress, J. Neurochem. 111 (2009) 882–889.
[40] I. Jang, et al., Genetic ablation and short-duration inhibition of lipoxygenase results in increased macroautophagy, Exp. Cell Res. 321 (2014) 276–287.
[41] M. Csala, et al., On the role of 4-hydroxynonenal in health and disease, Bba-Mol Basis Dis 1852 (2015) 826–838.
[42] H. Zhang, H.J. Forman, 4-hydroxynonenal-mediated signaling and aging, Free Radic. Biol. Med. 111 (2017) 219–225.
[43] M. Dodson, et al., Regulation of autophagy, mitochondrial dynamics, and cellular bioenergetics by 4-hydroxynonenal in primary neurons, Autophagy 13 (2017) 1828–1840.
[44] Ö. Canli, Glutathione peroxidase 4 regulates autophagy and cell death during erythropoiesis. http://mediatum.ub.tum.de/?id=1135408, 2013.
[45] M. Hamasaki, et al., Autophagosomes form at ER-mitochondria contact sites, Nature 495 (2013) 389–393.
[46] L. Ge, D. Melville, M. Zhang, R. Schekman, The ER-Golgi intermediate compartment is a key membrane source for the LC3 lipidation step of autophagosome biogenesis, Elife 2 (2013), e00947.
[47] D.W. Hailey, et al., Mitochondria supply membranes for autophagosome biogenesis during starvation, Cell 141 (2010) 656–667.
[48] B. Ravikumar, K. Moreau, L. Jahreiss, C. Puri, D.C. Rubinsztein, Plasma membrane contributes to the formation of pre-autophagosomal structures, Nat. Cell Biol. 12 (2010) 747–757.
[49] W.L. Yen, et al., The conserved oligomeric Golgi complex is involved in double-membrane vesicle formation during autophagy, J. Cell Biol. 188 (2010) 101–114.
[50] M. Mari, S.A. Tooze, F. Reggiori, The puzzling origin of the autophagosomal membrane, F1000 Biol Rep 3 (2011) 25.
[51] D.C. Rubinsztein, T. Shpilka, Z. Elazar, Mechanisms of autophagosome biogenesis, Curr. Biol. 22 (2012) R29–R34.
[52] Y. Sou, I. Tanida, M. Komatsu, T. Ueno, E. Kominami, Phosphatidylserine in addition to phosphatidylethanolamine is an in vitro target of the mammalian Atg8 modifiers, LC3, GABARAP, and GATE-16, J. Biol. Chem. 281 (2006) 3017–3024.
[53] J. Durgan, et al., Non-canonical autophagy drives alternative ATG8 conjugation to phosphatidylserine, Mol. Cell. 81 (2021) 2031–2040.
[54] L.W. Brier, et al., Regulation of LC3 lipidation by the autophagy-specific class III phosphatidylinositol-3 kinase complex, Mol. Biol. Cell 30 (2019) 1098–1107.
[55] F.M. Menzies, A. Fleming, D.C. Rubinsztein, Compromised autophagy and neurodegenerative diseases, Nat. Rev. Neurosci. 16 (2015) 345–357.
[56] R.L. Vidal, S. Matus, L. Bargsted, C. Hetz, Targeting autophagy in neurodegenerative diseases, Trends Pharmacol. Sci. 35 (2014) 583–591.
[57] E. Wong, A.M. Cuervo, Autophagy gone awry in neurodegenerative diseases, Nat. Neurosci. 13 (2010) 805–811.
[58] Y.M. Yao, C.M. Clark, J.Q. Trojanowski, V.M.Y. Lee, D. Pratico, Elevation of 12/15 lipoxygenase products in AD and mild cognitive impairment, Ann. Neurol. 58 (2005) 623–626.
[59] H. Yang, J.M. Zhuo, J. Chu, C. Chinnici, D. Pratico, Amelioration of the Alzheimer's disease phenotype by absence of 12/15-lipoxygenase, Biol. Psychiatr. 68 (2010) 922–929.
[60] A. Di Meco, et al., 12/15-Lipoxygenase inhibition reverses cognitive impairment, brain amyloidosis, and tau pathology by stimulating autophagy in aged triple transgenic mice, Biol. Psychiatr. 81 (2017) 92–100.
[61] Y. Fu, et al., Discovery of a small molecule targeting autophagy via ATG4B inhibition and cell death of colorectal cancer cells in vitro and in vivo, Autophagy 15 (2019) 295–311.

[62] D.K. Luci, et al., Synthesis and structure-activity relationship studies of 4-((2-hydroxy-3-methoxybenzyl)amino)benzenesulfonamide derivatives as potent and selective inhibitors of 12-lipoxygenase, J. Med. Chem. 57 (2014) 495–506.
[63] W. Li, et al., Autophagic degradation of PML promotes susceptibility to HSV-1 by stress-induced Corticosterone, Theranostics 10 (2020) 9032–9049.
[64] M.M. Julkowska, J.M. Rankenberg, C. Testerink, Liposome-binding assays to assess specificity and affinity of phospholipid-protein interactions, Methods Mol. Biol. 1009 (2013) 261–271.
[65] M. Li, X. Chen, Q.Z. Ye, A. Vogt, X.M. Yin, A high-throughput FRET-based assay for determination of Atg4 activity, Autophagy 8 (2012) 401–412.
[66] M.R. Wieckowski, C. Giorgi, M. Lebiedzinska, J. Duszynski, P. Pinton, Isolation of mitochondria-associated membranes and mitochondria from animal tissues and cells, Nat. Protoc. 4 (2009) 1582–1590.
[67] W.X. Wu, et al., FUNDC1 regulates mitochondrial dynamics at the ER-mitochondrial contact site under hypoxic conditions, EMBO J. 35 (2016) 1368–1384.
[68] J. Folch, M. Lees, G.H. Sloane Stanley, A simple method for the isolation and purification of total lipides from animal tissues, J. Biol. Chem. 226 (1957) 497–509.
[69] F.F. Hsu, J. Turk, Electrospray ionization with low-energy collisionally activated dissociation tandem mass spectrometry of glycerophospholipids: mechanisms of fragmentation and structural characterization, J. Chromatogr., B: Anal. Technol. Biomed. Life Sci. 877 (2009) 2673–2695.
[70] R.C. Murphy, P.H. Axelsen, Mass spectrometric analysis of long-chain lipids, Mass Spectrom. Rev. 30 (2011) 579–599.